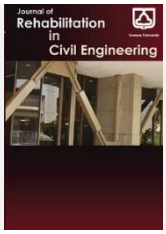

Journal of Rehabilitation in Civil Engineering

Journal homepage: https://civiljournal.semnan.ac.ir/

In-Plane Static Cyclic Response of Solid Brick Masonry Walls Repaired and Retrofitted with TRM

Hamid Assarzadeh Mahani [1]; Mohammad Yekrangnia [2,*]; Mussa Mahmoudi [3]

1. Ph.D. Candidate, Department of Civil Engineering, Shahid Rajaee Teacher Training University, Tehran, Iran
2. Associate Professor, Faculty of Civil Engineering, Shahid Rajaee Teacher Training University, Tehran, Iran
3. Professor, Faculty of Civil Engineering, Shahid Rajaee Teacher Training University, Tehran, Iran
* Corresponding author: *yekrangnia@sru.ac.ir*

ARTICLE INFO

Article history:
Received: 09 May 2025
Revised: 20 August 2025
Accepted: 23 December 2025

Keywords:
Masonry walls;
Cyclic shear compression test;
Textile Reinforced Mortar (TRM);
Seismic strengthening;
Ductility;
DIC;
Numerical analyses;
Analytical predictions.

ABSTRACT

This study demonstrates that Textile-Reinforced Mortar (TRM) systems offer a practical, cost-effective, and sustainable solution for improving the seismic safety of unreinforced masonry (URM) walls, both for post-earthquake repair and preventive retrofitting. TRM significantly enhances load-bearing capacity, ductility, and energy dissipation, addressing the urgent need for resilient and compatible strengthening techniques in earthquake-prone areas. Experimental results reveal that TRM reinforcement increases in-plane load-bearing capacity by 180% in repaired walls and up to 230% in retrofitted walls compared to unreinforced specimens. Displacement capacity under cyclic loading improves by 35% for repaired and 20% for retrofitted walls, while ductility, shear strength, and energy dissipation improve by factors of up to 5.0, 4.8, and 1.1, respectively. Digital image correlation (DIC) and finite element modeling confirm a shift in failure mode from shear to flexure-dominated mechanisms, resulting in more uniform crack distribution and reduced local damage concentration. Comparison with theoretical models such as ACI 549.4R-20 and Eurocode 8 validates the reliability of the methods used. These findings provide engineers and practitioners with a robust, evidence-based framework to select and design TRM interventions that enhance the seismic resilience of both existing and new masonry structures, especially in high seismic risk regions.

E-ISSN: 2345-4423
© 2026 The Authors. Journal of Rehabilitation in Civil Engineering published by Semnan University Press.
This is an open access article under the CC-BY 4.0 license. (https://creativecommons.org/licenses/by/4.0/)

How to cite this article:
Assarzadeh Mahani, H., Yekrangnia, M. and Mahmoudi, M. (2026). In-Plane Static Cyclic Response of Solid Brick Masonry Walls Repaired and Retrofitted with TRM. Journal of Rehabilitation in Civil Engineering, 14(3), 2309 https://doi.org/10.22075/jrce.2025.2309

1. Introduction

Unreinforced masonry (URM) buildings constitute a substantial portion of the built environment in Iran and the Middle East, especially in historic urban centers vulnerable to earthquakes [1–3]. These buildings, typically erected without seismic detailing, exhibit significant brittle failure, low ductility, and poor energy dissipation under lateral loads—shortcomings that have been tragically exposed in recent seismic events. Given the scarcity of land and the high concentration of heritage buildings, conventional retrofit strategies (e.g., reinforced shotcrete, steel jacketing, and epoxy-based FRPs) are often unsuitable due to invasiveness, weight, and compatibility issues [1],[4–9].

In this context, Textile Reinforced Mortar (TRM) has emerged as a viable, lightweight, and compatible alternative for seismic strengthening and post-earthquake repair of masonry walls. TRM systems, consisting of high-strength fiber textiles embedded in an inorganic mortar matrix, improve shear strength, deformability, and energy dissipation in masonry walls, as demonstrated by multiple experimental campaigns [10–12]. Moreover, TRM exhibits superior environmental durability, especially with glass or carbon fibers, and is more compatible with historic masonry fabric than polymer-based composites. Despite these advances, most TRM research has focused on undamaged masonry specimens, while the performance of repaired walls—realistically representing post-earthquake intervention scenarios—remains understudied. The mechanisms of load transfer, crack redistribution, and interfacial bond in repaired substrates are fundamentally different from those in pristine walls, owing to residual damage, degraded interfaces, and stress concentrations. Prior work on pre-damaged confined masonry walls reinforced with carbon-glass hybrid TRM highlighted the influence of textile arrangement, pre-compression, and substrate repair quality on structural response; however, analytical models often overestimate post-repair capacity due to idealizations about interface behavior [13,14].

Furthermore, in-plane failure modes in TRM-strengthened masonry walls vary with wall aspect ratio, pre-compression, and textile layout: flexural (rocking/toe crushing) dominates in slender walls, while shear (diagonal cracking) governs in squat walls. Mixed modes are often observed at intermediate aspect ratios, where TRM-substrate interaction plays a decisive role in ultimate behavior.

Existing design guidelines—including ACI 549.4R-20 [15], CNR-DT 215 [16], Eurocode 8 [17], and models by Triantafillou and Bournas [18,19]—generally predict the behavior of undamaged improved walls well but are less reliable for repaired substrates. Discrepancies between model predictions and experiments persist, particularly in cases involving cyclic loading and prior damage, necessitating further validation via detailed experimental and numerical studies tailored to region-specific materials and construction practices.

This study fills this critical gap through a comprehensive experimental and numerical investigation of 2:3-scale unplastered solid brick URM walls in three configurations: unreinforced, repaired with glass TRM (G-TRM), and retrofitted with G-TRM. In-plane reversed cyclic shear-compression tests simulated realistic seismic loading, while Digital Image Correlation (DIC) provided detailed strain mapping and failure mechanism tracking. Parametric finite element modeling in ABAQUS [20] was calibrated against test data to explore the influence of key design variables (overlay thickness, pre-compression).

The results offer novel insights into the efficacy of TRM for both retrofit and repair, validating its potential as a code-compliant and practically feasible solution for URM structures in high-seismicity regions. By bridging the gap between laboratory evidence and real-world practice, this research supports the development of regional retrofit and repair guidelines and aids in protecting vulnerable communities while preserving cultural heritage for future generations.

2. Research gap and novelty

2.1. Research gap

Existing TRM research predominantly focuses on retrofitting undamaged URM walls, leaving the seismic behavior of damaged and repaired walls significantly underexplored despite its critical real-world need in earthquake zones. Systematic experimental and numerical evaluations of TRM specifically as a repair method for damaged walls are scarce. Furthermore, few studies integrate cyclic testing, advanced DIC crack monitoring, detailed micro-modeling, and direct analytical comparisons between both retrofitted and repaired walls under standardized conditions.

2.2. Novelty of the current study

This study presents the first comprehensive investigation comparing the in-plane cyclic performance of TRM-repaired (post-damage) and TRM-retrofitted (undamaged) solid brick masonry walls under identical conditions. It integrates experimental cyclic testing with DIC analysis, validated micro-modeling, and analytical predictions (ACI 549.4 [21], Eurocode 8 [22], CNR-DT 215 [16]) to quantify strength, ductility, displacement capacity, and energy dissipation for both cases versus unreinforced benchmarks. By directly evaluating repair efficacy against conventional retrofit, it addresses a critical seismic engineering gap—determining if TRM repair can restore lost performance after earthquakes. The parametric analyses and synthesis of methods enable reliable, conservative design guidance for cost-efficient post-earthquake strategies.

3. Experimental program

This experimental study was conducted at the Structural Laboratory of Shahid Rajaee Teacher Training University in Iran. The primary objective was to evaluate the effectiveness of TRM in enhancing the seismic performance of unreinforced masonry walls. The research focused on in-plane shear-compression tests to assess the improvements in strength and durability of URM walls reinforced with TRM under seismic loading conditions.To provide a clear overview of the systematic approach followed in this study, Figure 1 presents a comprehensive flowchart illustrating the main experimental , numerical ,and analytical steps undertaken.

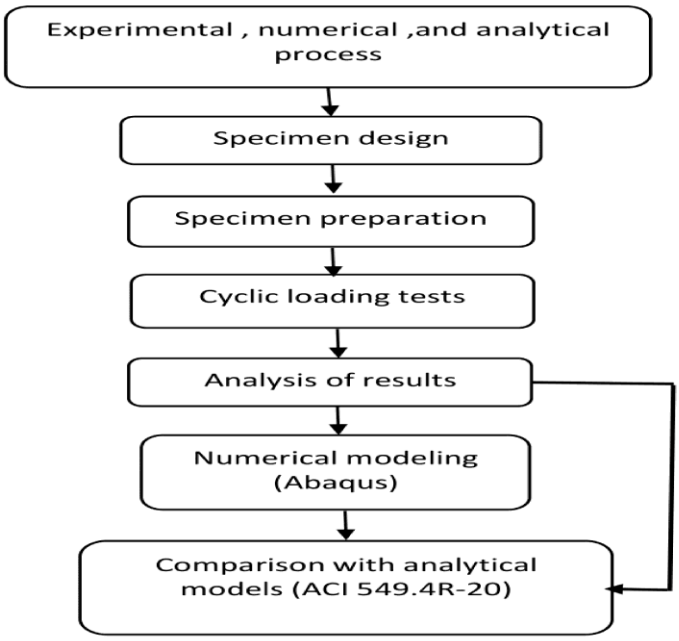

Fig. 1. Process flow chart of the present study.

3.1. Test specimens

Two types of the URM wall specimens were constructed using solid clay bricks and cement-sand mortar with joint widths of approximately 16 mm. The first, designated as the reference specimen, measured 2500 × 1500 × 205 mm (see Figure 2) and underwent damage, repair, and retrofitting to simulate the behavior of an existing URM structure. The second specimen, with identical dimensions, was retrofitted using G-TRM. Both specimens were built at a reduced scale of 2:3, featuring an aspect ratio (height-to-length) of 0.6.

The specimens were subjected to cyclic in-plane lateral displacements while under a constant vertical (gravity) load during testing. To ensure enhanced stability, the walls were anchored to the foundation using glass mesh embedded in mortar.

A series of three wall specimens-including reference, repaired, and retrofitted configurations-were constructed following the specifications outlined in Table 1. These walls were designed to replicate typical unreinforced masonry buildings in Iran and were tested under controlled laboratory conditions to evaluate their structural performance under the prescribed loading protocols.

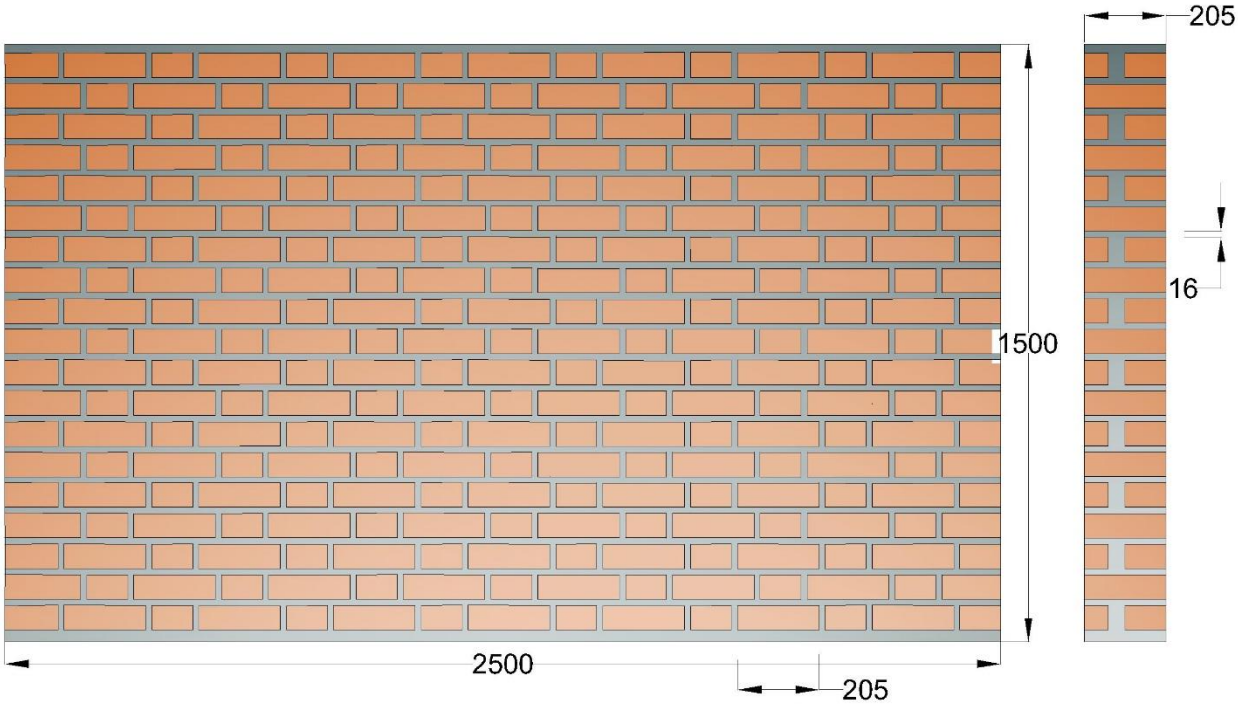

Fig. 1. Wall geometry (values in mm) and Flemish bond pattern in brick masonry.

Table 1. Unreinforced and TRM-repaired and retrofitted walls.

Specimen	Strength method			Thickness of overlay (mm)
	URM	Retrofitted	Repaired	
URM	✓			
Re1-15			✓	15
R1-15		✓		15

In this study, ‘Re1-15’ refers to the wall specimen that was first damaged and then repaired and strengthened with a single layer of TRM comprising glass fiber mesh and a 15-mm mortar overlay, while ‘R1-15’ denotes the wall specimen that was retrofitted with the same TRM system prior to any damage.

3.2. Materials

3.2.1. Masonry prism, mortar, and brick

The solid clay bricks used in this study measured approximately 210 × 105 × 60 mm. Their compressive strength was determined by testing six specimens in accordance with ASTM C67-02C [23] standards. The average compressive strength was approximately 8.7 MPa, with a coefficient of variation (COV) of 1.9 MPa. Additionally, compression and shear tests were conducted on the masonry specimens, as illustrated in Figure 3. The masonry walls were constructed using a cement-sand mortar with a cement-to-sand ratio of 1:5 and a joint thickness of 16 mm. The water content in the mortar was carefully controlled to ensure optimal workability. Detailed material properties are summarized in Table 2.

Table 1. Material Specifications.

Name of material	Property	No of specimens	Reference	Mean value (COV (Coefficient of Variation) (%))
Bricks	Dimension (mm)	6	ASTM C 134 – 95 [24]	204×100×57 (5)
	Water absorption (%)	6	ASTM C 134 – 95 [24]	17.2 (6)
	Density (kg/m^3)	6	ASTM C 134 – 95 [24]	1910 (12)
	Compressive strength (MPa)	6	ASTM C-67 [23]	8.7 (1.9)
	Modulus of elasticity (MPa)	6	ASTM C109/C109M [25]	3931 (15)
	Flexural Strength (MPa)	6	ASTM C 1072 [26]	4.6 (25)
Cement-sand mortar	Compressive Strength (MPa)	6	ASTM C109/C109M [25]	9.6 (10)
	Shear Strength (MPa)	6	BS EN 1052-3 [27]	0.2 (15)
	Friction Coefficient	6	BS EN 1052-3 [27]	0.7 (15)
Masonry prism	Compressive Strength (MPa)	6	ASTM C1314-02A [28]	5.9 (16)
Mortar Overlay with fiber (MF)	Compressive strength (MPa)	6	EN 1015–11 [29]	16.5 (22)
	Tensile strength (MPa)	6	ASTM C348 [30]	2.1 (14)
Mortar Overlay without fiber (MW)	Compressive strength (MPa)	6	EN 1015–11 [29]	15.5 (15)
	Tensile strength (MPa)	6	ASTM C348 [30]	1.6 (12)

a) b)

Fig. 2. Experimental tests: a) Compression and b) Shear tests on masonry specimens.

3.2.2. Overlay mortar, AR. glass textile mesh

3.2.2.1. Overlay mortar

The composition of the overlay mortar used in the TRM system is detailed in Table 3.

Table 2. Mix proportions of overlay mortar.

Material	Proportion (kg/m^3)
Fine Sand (0-0.6 mm)	958
Cement	798
Water	335
Microgel*	96
Polypropylene (P.P). fiber*	13
Silica Fume*	80

*Manufactured by Shimi Sakhteman Co.(https://www.shimisakhteman.com)

3.2.2.2. AR-glass mesh

The use of AR glass textile for TRM was chosen due to its superior alkali resistance in cementitious matrices, favorable cost–performance ratio, wide availability, and proven effectiveness in enhancing the seismic performance of masonry walls. The textiles studied consist of alkali-resistant (AR) glass rovings woven from filaments of varying diameters. Tensile tests were conducted on three types of AR glass rovings to evaluate their mechanical properties, as illustrated in Figure 4. Detailed geometric and mechanical properties of these textiles are summarized in Table 4.

Table 3. Mechanical properties and textile geometric.

Fiber Type	No. of Filaments per yarn	Filament Tensile Strength (MPa)	Filament elasticity modulus (GPa)	Filament break extension (%)	Yarn density (g/cm^3)
AR-Glass	4000	995	73	2.5	2.58

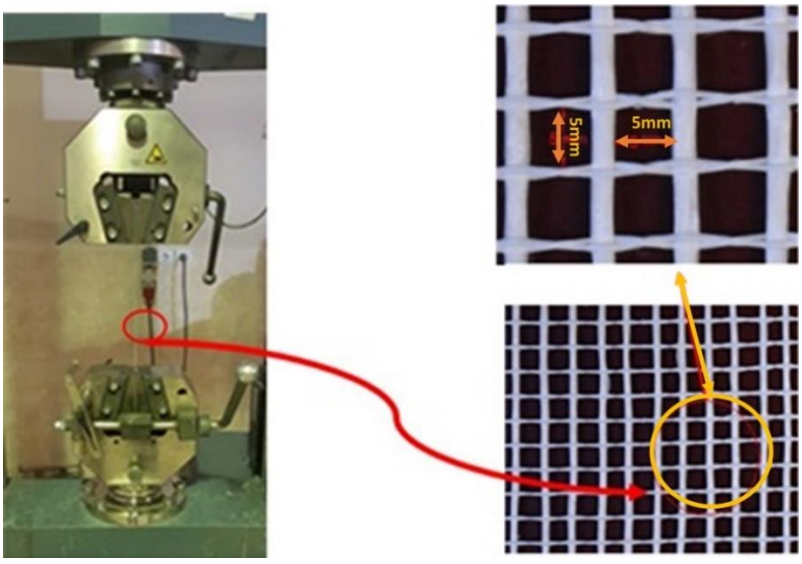

a) b)

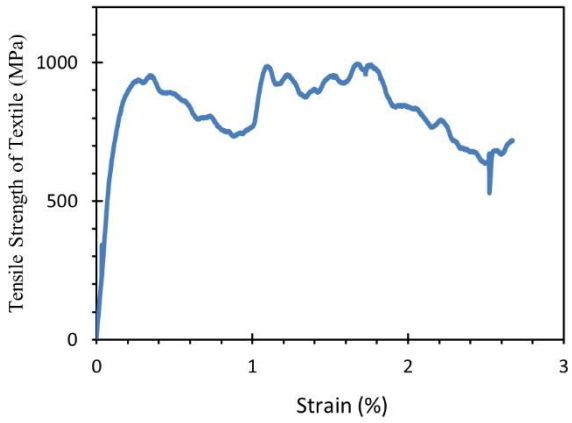

c)

Fig. 3. Fiber bundle a) Test setup b) Geometrical configurations c) Tensile strength of AR-glass mesh versus strain curve.

3.3. Shear strength of bed joint

The bed joint shear test was performed on masonry prisms constructed with solid clay bricks and cement-sand mortar. A constant vertical pre-compression was applied, and the lateral load was gradually increased

parallel to the bed joint until failure. This setup allowed direct measurement of the shear strength at the brick-mortar interface, which is essential for characterizing the in-plane behavior of masonry walls under seismic actions.The shear strength of the bed joint was assessed using three designated samples-URMW-1, URMW-2, and URMW-3-in accordance with the guidelines of UNI EN 1052-3 (2007) [27], as illustrated in Figure 3-b.

Based on the experimental triplet tests performed in this study, the average initial bed joint shear strength was measured at 0.2 MPa, which was used as the allowable value for analytical comparisons and capacity calculations.

3.4. Implementationof textile-reinforced mortar (TRM)

TRM implementation involves applying mortar-textile-mortar layers on existing masonry or concrete surfaces after appropriate preparation. The textile mesh acts as internal reinforcement, and the mortar binds it to the substrate, creating a composite system that improves structural performance, especially under seismic loads. Figure 6 presents a flowchart outlining the sequential steps for applying Textile-Reinforced Mortar (TRM) to retrofit or repair unreinforced masonry walls. Key steps include substrate preparation, crack repair, sequential application of mortar and mesh, and quality curing. This process ensures optimal bond, crack-bridging, and strengthening of existing masonry structures.

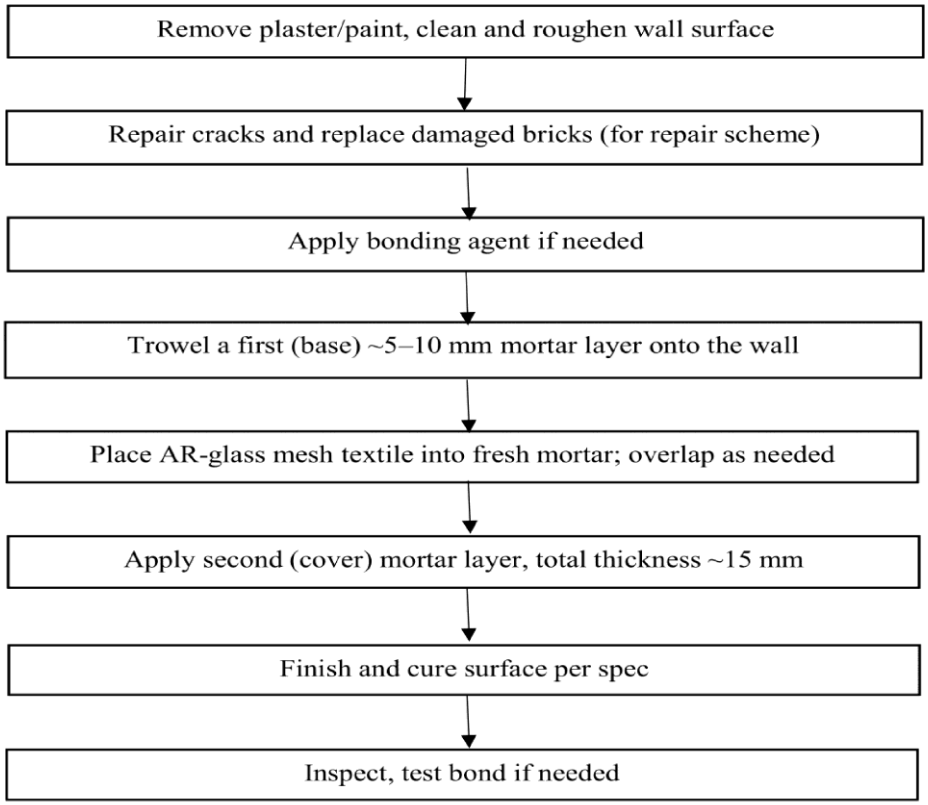

Fig. 4. Process flow chart of the step-by-step application of Textile-Reinforced Mortar (TRM) for retrofitting or repairing unreinforced masonry walls [15].

3.5. Test setup

The specimens were tested using the setup illustrated in Figure 6, which was constructed on a prefabricated reinforced concrete foundation. A 100 kN hydraulic actuator applied a constant vertical load, while a 1000 kN horizontal hydraulic jack imposed cyclic in-plane lateral loads. A rigid steel beam was used to distribute the vertical load evenly across the top of the specimen, and lateral bracing was incorporated to prevent out-of-plane displacement.

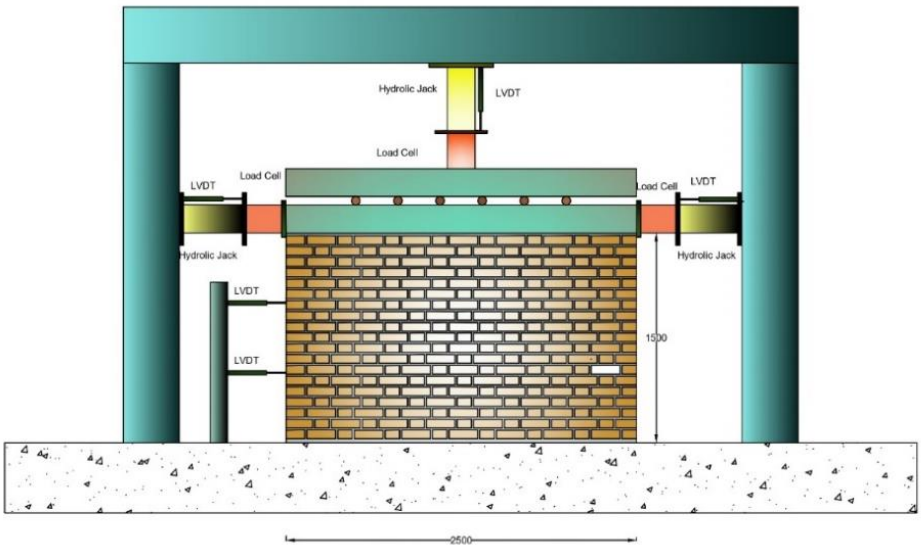

Fig. 5. Test setup.

3.6. Loading procedure

The study employed a cyclic loading protocol based on ASTM E2126-02a [31] to perform quasi-static tests simulating seismic effects on unreinforced masonry walls. The protocol involved incremental drift cycles with increasing deformation amplitudes, applying at least three fully reversed push-pull cycles at each level. This method realistically models repeated earthquake shaking, allowing for accurate assessment of accumulated damage, failure mechanisms, and key seismic performance indicators such as ductility, energy dissipation, and damage progression.The test commenced with the application of vertical loads and the installation of sensors, followed by cyclic displacements imposed via a horizontal actuator (1000 kN capacity, 1 mm/s displacement rate). Constant vertical axial loads of 40 kN were applied in force-control mode to specimens URM, Re1-15, and R1-15 to replicate typical gravity loads corresponding to a one-story masonry building, resulting in an axial compressive stress of approximately 0.07 MPa. Subsequently, cyclic in-plane lateral loads were applied at the top of the specimens in displacement-control mode to simulate earthquake effects, following a low-rate loading pattern as illustrated in Figure 7.

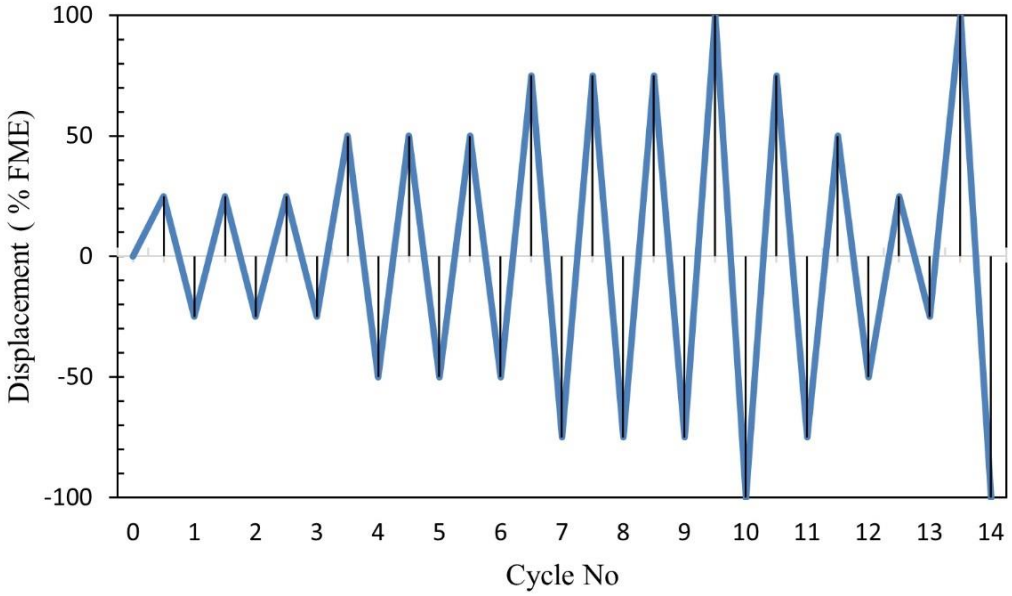

Fig. 6. Loading protocol and cyclic displacement schedule (test method A).

3.7. Monitoring strategy

Figure 7 shows the setup of four LVDTs to monitor horizontal and vertical displacements and three load cells to measure vertical and horizontal loads on GTRM-strengthened brick masonry walls. Digital image correlation (DIC) with a high-resolution camera and ARAMIS 3D software was used to track failure progression. Displacement control was applied during testing, with load cells at the top, top-left, and top-right, and LVDTs at the top-center, top-left, and top-right. An automated data acquisition system recorded load and displacement. DIC parameters (subset = 21 pixels, step = 5 pixels) were optimized through preliminary tests, and calibration against LVDTs confirmed sub-millimeter accuracy. This method provided reliable strain and crack detection on masonry surfaces.

3.8. Experimental observations

The study evaluated the effectiveness of a TRM layer in strengthening both intact and damaged masonry walls subjected to in-plane shear forces. Key results from these three cases are summarized in Table 5. quantifies the substantial improvements in seismic performance parameters—strength, ductility, energy dissipation, and stiffness retention—achieved through TRM repair and retrofit. These results provide tangible evidence for the efficacy of TRM interventions in both restoring and enhancing the seismic resilience of masonry walls, offering valuable benchmarks for engineering practice and future code development.

Table 4. Specimen behavior.

Specimen	Envelope	Crack limit state		Peak resistance limit state		Ultimate limit states	Energy dissipation (kN.mm)	Displacement ductility	Failure mode
		Lateral drift (%)	Lateral strength (kN)	Lateral drift (%)	Lateral strength (kN)	Lateral drift (%)	Lateral strength (kN)			
URM	Push	0.02	24.5	0.05	36.0	0.1	28.0	271.9	3.1	Shear sliding
	Pull	0.02	-24.5	-0.06	-38.0	-0.1	-28.0	271.2	3.2	
Re1-15	Push	0.20	44.1	0.60	63.0	0.86	56.7	543.3	3.4	Toe crushing, shear sliding
	Pull	-0.25	-35.0	-0.60	-50.0	-0.97	-45.0	501.1	3.0	
R1-15	Push	0.35	70.9	0.50	101.3	1.08	91.2	1963.0	2.4	Toe crushing, shear sliding
	Pull	-0.40	-67.9	-0.80	-97.0	-0.87	-87.3	640.6	1.7	

3.8.1. Assessment of cracking

The images presented in Figure 8 depict the crack patterns and the maximum crack width (Wc) measured in the damaged specimens at the conclusion of the tests. Specimens Re1-15 and R1-15 exhibited a uniform distribution of cracks, highlighting the effectiveness of the strengthening technique in promoting even damage dispersion throughout the wall and thereby reducing the concentration of damage along any single crack.

a) b) c)

Fig. 7. Pictures of the crack distribution on the walls at ultimate mode: a) URM, Wc=15mm b) Re1-15, Wc=12mm c) R1-15, Wc=10mm.

3.8.2. Cyclic behavior of specimens

Figure 9 presents the hysteresis curves for three wall types: the reference URM wall, the repaired wall (Re1-15), and the retrofitted wall (R1-15). The vertical axis represents the applied force (kN) at the top steel beam under cantilever loading, while the horizontal axis corresponds to the in-plane horizontal displacement, d (mm).

In the retrofitted specimens, the first visible crack consistently occurred at the masonry-concrete foundation interface (Figure 9), identifying this bond as the critical failure interface. This early separation caused a transition in structural response from shear-dominated behavior to a rocking mechanism. Strengthening with TRM altered the failure mode from shear to flexural-dominated mechanisms, characterized by rigid-body rotation, often coupled with secondary failure types. A full TRM system with continuous anchorage at both the rooftop and foundation-or across multiple stories-could significantly improve performance by preventing premature wall-base separation.

The TRM-strengthened specimens exhibited hysteretic behavior characterized by minimal strength degradation and limited hysteretic energy dissipation, forming a distinctive flag-shaped hysteresis pattern, which is typical of rocking-dominated systems. This hysteresis shape is characterized by sharp drops in load followed by near-vertical reloading branches, resembling a flag. It indicates minimal residual deformation and suggests that the structure primarily dissipates energy through opening and closing of cracks, rather than plastic yielding. These observations align with findings from prior studies [32,33].

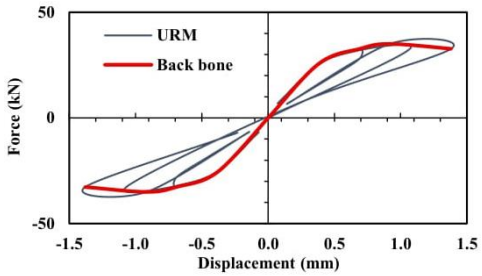

a)

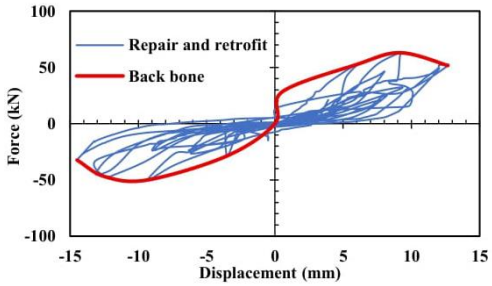

b)

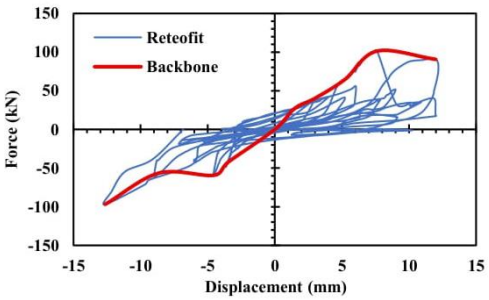

c)

Fig. 8. Force-displacement hysteresis and envelop curves: a) URM, b) Re1-15, and c) R1-15 walls.

The specimens were exposed to cyclic push-pull loading through a horizontal hydraulic actuator installed at the upper section of the walls, aligned with their longitudinal axis.These cycles involved the application of pulling (negative displacement) and pushing (positive displacement) forces on the specimens, as illustrated in Figure 6.

A load cell was used to monitor the horizontal load that the hydraulic actuator applied during the displacement control tests. As illustrated in Figure 9, the walls initially exhibited symmetrical hysteresis loops, demonstrating consistent bidirectional load-displacement responses during early cycles.

The unreinforced wall failed under pulling loads, while the Re1-15 specimen failed under pushing loads but showed a 77% increase in load-bearing capacity and enhanced displacement capacity (final displacements ≈ +9.2 mm, –9.3 mm). The R1-15 specimen behaved similarly initially but achieved 61% higher load-bearing capacity in the pushing direction and withstood displacements up to +11 mm. In both strengthened specimens, tests ended after failure in the pushing direction despite higher expected drift in pulling. Overall, GTRM strengthening significantly improved load-bearing strength, displacement capacity, and post-failure ductility compared to the unreinforced masonry wall. All specimens exhibited hysteresis loops with a pinching effect, indicating reduced hysteretic energy dissipation under cyclic loading. This behavior, common in systems like confined masonry walls, results from material degradation due to shear stresses. Pinching is mainly caused by crack cycling, interface slip, and TRM debonding, which lower reloading stiffness and energy dissipation. While TRM strengthening improved performance, pinching still occurred. Future work should focus on improved mortars, surface preparation, and anchorage methods to further reduce pinching and enhance energy dissipation.

3.8.3. Mechanical and envelopes performance

Figure 10 shows envelope curves for pulling and pushing directions derived from hysteretic peak loads and drift displacements. The curves are largely symmetrical up to a drift threshold, after which progressive deterioration causes failure. GTRM-strengthened specimens (Re1-15 and R1-15) showed gradual peak-load reduction with increasing displacement under pushing forces, reaching critical displacements of about +3.8 mm (Re1-15) and +5.25 mm (R1-15), and maximum displacements up to +16.2 mm. Strength degradation along the pulling direction was minimal, though stiffness decreased with increasing displacement. Initial stiffness was similar for URM and Re1-15 but lower for R1-15, likely due to delayed engagement of the TRM overlay, bonding imperfections, and limited early-stage deformation. Re1-15's repair process may have enhanced interlock and stress redistribution, leading to higher initial stiffness. Similar trends have been observed in prior TRM retrofitting studies [34,35].

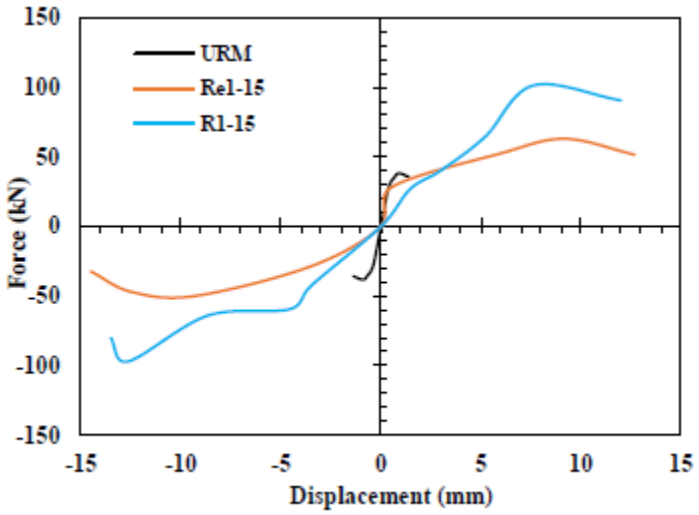

Fig. 9. Envelop curves of tested specimens.

As previously noted, one specimen served as the unretrofitted reference, while the other two specimens exhibited characteristics similar to the reference. The retrofitted and repaired specimens were compared against this baseline specimen. The hysteresis envelope curves were idealized following the guidelines outlined in FEMA 356 [36] and ASCE 41 [37]. Key hysteretic properties-including yield strength, maximum strength, displacement ductility, and effective stiffness-were determined using the equivalent bilinear approximation for all specimens.

By definition, the initial stiffness, K_i, is the experimental envelope curve gradient at the origin. Conversely, effective stiffness, K_e, is defined as ductility of displacement, as per Eq.(1), have unique definitions.

$$K_e = \frac{V_y}{\delta_y} \quad (1)$$

where d_m, d_y, and V_y denote displacement at maximum, yield displacement, and yield strength, respectively.

3.8.4. Strength and stiffness degradation

By definition, the examination of the rigidity of masonry walls focuses on the secant stiffness, which is the correlation between 70% of the peak load experienced during a cycle and the corresponding displacement [38–40]. The hysteresis curves illustrate a reduction in secant stiffness as the applied displacement increase. Within the literature, certain researchers [41,42] have shown increasing interest in investigating the secant stiffness at each iteration, subsequently standardizing it relative to the secant stiffness observed at the point of maximum load. Several authors, such as [43,44], have suggested different methods for determining the initial stiffness, $K_{initial}$. It is commonly described as the secant stiffness at 15% of the peak force on the experimental curve and signifies the stiffness of the uncracked portion of the sample. The progression of stiffness relative to displacement for each cycle is illustrated in Figure 11.

Figure 12 presents a graphical representation of the stiffness of the unreinforced wall relative to a normalized residual value, facilitating comparison. Upon visual examination, it was noted that there was no damage in the initial elastic phase. Moreover, the specimens reinforced with GTRM exhibited a degradation trend similar to that depicted in Figure 9.

The analysis of experimental findings also involves assessing strength reduction, a crucial aspect. ASTM-E-2126-02a [31] stipulates the differentiation between cyclic and in-cycle deteriorations. Cyclic strength reduction refers to the decline in strength between cycles conducted with the same displacement amplitude. One approach to evaluating structural damage involves determining stiffness reduction over cycles, as referenced in [40]. The method involves assessing lateral stiffness at multiple lateral displacement stages during the first cycle of each displacement amplitude within the in-plane loading protocol. Displacement-level stiffness is calculated as the secant stiffness corresponding to each cycle's the peak force, accounting for both directions (positive and negative).This calculation method, detailed in reference [45] and represented in Eq.

$K_{ei} = H^{+i} - H^{-i}\delta^{+i} - \delta - i$ (2), is essential for comprehending structural response and performance under cyclic loading conditions.

$$K_{ei} = \frac{H^{+i} - H^{-i}}{\delta^{+i} - \delta^{-i}} \quad (2)$$

For cycle i, the peak forces recorded in the negative and positive directions are represented as $H\text{-}i$ and $H+i$, respectively. These forces are paired with their corresponding displacements, $\delta{-}i$. (negative direction) and $\delta{+}i$ (positive direction).

Figure 12 shows that secant stiffness decreases as lateral displacement increases. Residual lateral stiffness, expressed as a percentage of the initial stiffness (K_initial), drops even during the uncracked phase. Despite no visible cracks, this reduction is attributed to internal microcracks forming at the mortar–brick interface, which are not detectable through visual inspection or the available instrumentation.

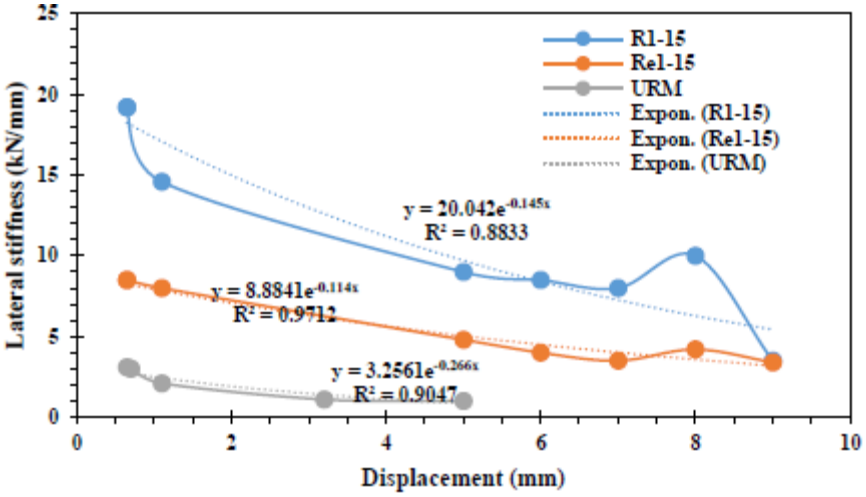

Fig. 10. Lateral stiffness vs displacement on SCT.

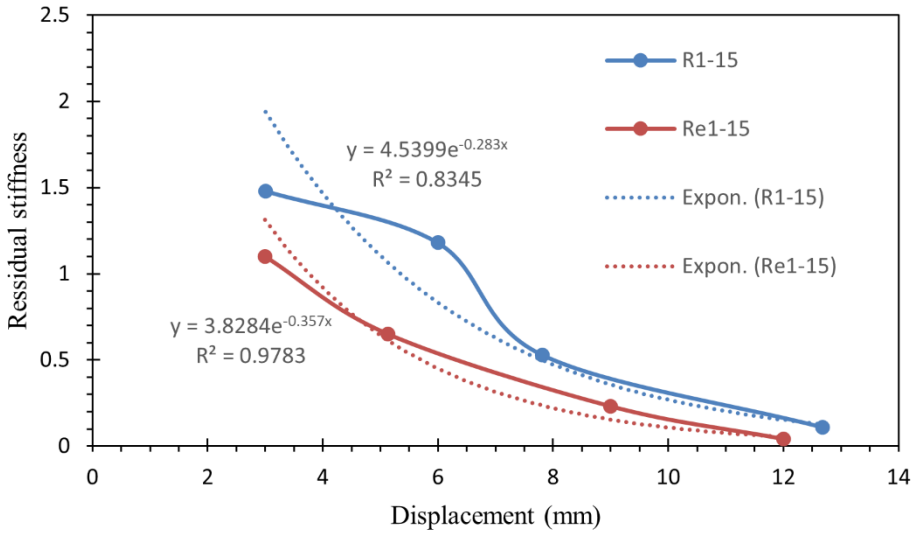

Fig. 11. The lateral stiffness degradation in the walls tested on SCT.

3.8.5. Energy dissipation capacity

The resilience of masonry buildings against seismic forces is largely dependent on their capacity to absorb and release energy. The integral method was employed using mathematical software named Webplotdigitizer to calculate the dissipated energy for each half-cycle (Ei). The specific coefficients necessary for this calculation are outlined in Table 6. Additionally, Figure 13 offers a visual depiction of the total energy dissipated (Et) during seismic activity. To further analyze the structural response to seismic forces, the equivalent viscous damping coefficient (ζeq) was determined using Eq.(3).

$$\zeta eq = \frac{Ei}{2\Pi \times \Delta i,max \times Vi,max} \tag{3}$$

The viscous damping coefficient (ζeq) was calculated from hysteretic energy, maximum displacement, and maximum shear force, with results summarized in Table 6. Both strengthened specimens showed decreasing damping as damage progressed. EC8 [22] recommends a damping ratio of 5–10%, and strengthened walls mostly fell within this range but occasionally exceeded 10%. The unreinforced wall exhibited higher damping, reaching about 2.2% at small displacements but degrading rapidly with damage. Overall, the URM specimen had greater equivalent damping than Re1-15 and R1-15 due to its wider crack distribution, which increased energy dissipation.

Table 5. Summary of dissipated hysteretic energy, drift, and equivalent viscous damping coefficients.

Half cycle	URM			Re1-15			R1-15		
	Energy (kN.mm)	Drift (%)	ζ (%)	Energy (kN.mm)	Drift (%)	ζ (%)	Energy (kN.mm)	Drift (%)	ζ (%)
1	47.90	0.07	3.4	3.96	0.30	2	24.40	0.30	3
2	47.10	0.11	2.2	1.03	0.21	1	21.95	0.30	7
3	112.00	0.14	4.0	8.95	0.39	2	25.20	0.15	10
4				15.00	0.35	2	0.50	0.30	1
5				59.10	0.62	5	48.20	0.40	5
6				22.40	0.62	2	25.50	0.36	2
7				75.30	0.60	4	65.51	0.51	5
8				30.00	0.63	3	40.70	0.45	2
9				46.80	0.93	3	39.20	0.77	2
10				25.92	0.88	2	85.20	0.59	6
11				55.30	1.20	2	75.00	1.08	3
12				106.92	1.25	3	117.40	0.90	3
13				22.80	0.78	2	80.00	0.90	3
14				100.00	0.93	3	31.00	0.53	6
15				29.10	0.82	2	181.70	0.60	9
16				107.00	0.90	8	17.00	0.71	2
17				164.30	0.92	5	76.60	0.64	9
18				53.80	1.45	2	27.20	0.71	3
19				9.00	1.27	1	400.50	1.20	6
20				39.00	1.31	1	28.30	0.54	11
21				68.70	0.80	3	429.80	0.76	9
22							245.40	1.27	3
23							517.30	2.53	3

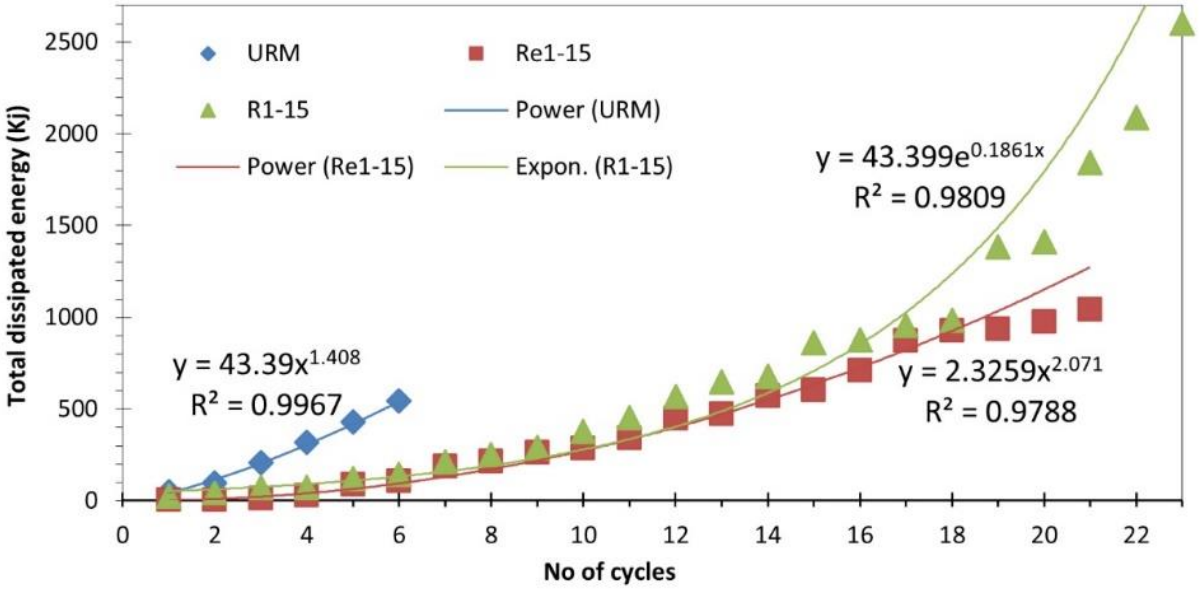

Fig. 12. Total dissipated energy versus each cycle.

3.8.6. Lateral displacement ductility

While the previous section highlighted a significant reduction in stiffness observed in the URM test at low drift values, which adversely affected the element's overall stability, this section focuses on assessing

ductility for individual specimens. Ductility (μ) is computed via Eq.(4), where δy corresponds to the displacement at initial cracking and δu is the ultimate lateral displacement attained in each specimen. To establish δy polygonal curves were derived from the envelope curves illustrated in Figure 14, adhering to the methodology described in. By pinpointing three crucial points, the polygonal curves were established; the points are (i) the point of maximum strength, (ii) the onset of first cracking, and (iii) the ultimate state.

$$\mu = \frac{\delta_u}{\delta_y} \tag{4}$$

The ductility outcomes for all specimens are detailed in Table 5. Significantly, the R1-15 specimen, reinforced with a GTRM layer, exhibited a ductility improvement surpassing 10% in the pushing direction.

This finding is particularly significant for the previously damaged wall, suggesting that GTRM restored the original capacity and also improved it by more than threefold, matching the retrofitted wall capacity that had no initial damage. However, in terms of the pulling direction, both the Re1-15 and R1-15 specimens had the potential to withstand higher loads and endure larger displacements. Yet, due to the occurrence of failure in the pushing direction, it was considered unsafe to induce failure in the opposite direction. Consequently, the ductility values obtained in the pulling direction do not provide a reliable indication, which could have been considerably higher.

3.8.7. DIC results

DIC contour maps (Figure 14,15) quantified in-plane displacements across all specimens, revealing distinct deformation patterns. Crack development in the URM wall proceeded rapidly, with diagonal cracks widening to 6 mm (average) and up to 8 mm (maximum), leading to abrupt strength loss. By contrast, GTRM reinforcement (Re1-15, R1-15) reduced maximum crack widths by 52–58% (to 16–19 mm) through effective crack bridging, which also promoted more uniform strain distribution. Strain localized progressively at key monitoring points (1–4), yet the GTRM layer showed 35% lower strain gradients than URM at failure. The tensile stresses mobilized in the GTRM delayed crack growth by 40% compared to the unreinforced case (Figure 14), and enhanced the specimen's strain redistribution capacity by a factor of 2.1. As a result, GTRM-retrofitted walls transitioned from brittle fracture to a more ductile, controlled damage mode. These results quantitatively demonstrate the effectiveness of GTRM in improving deformation capacity and crack control, in line with prior findings for similar TRM systems.Additionally, it is critical to highlight that during loading, the externally applied load directly impacted the wall, while the TRM strengthening layer passively resisted these forces.

This configuration caused stress to transfer sequentially from the inner matrix material, through the textile reinforcement, to the outer matrix layer. As a result, accounting for the strain lag effect is essential. This effect refers to the delay or mismatch between the internal strain distribution within the masonry-TRM system and the strain measured on the outer mortar surface. It arises because the TRM system transfers load from the inner masonry through the textile mesh to the outer matrix, resulting in potential underrepresentation of true internal stresses in surface measurements obtained via DIC. The inherent heterogeneity of the matrix material further complicates analysis, requiring careful interpretation of deformation patterns.

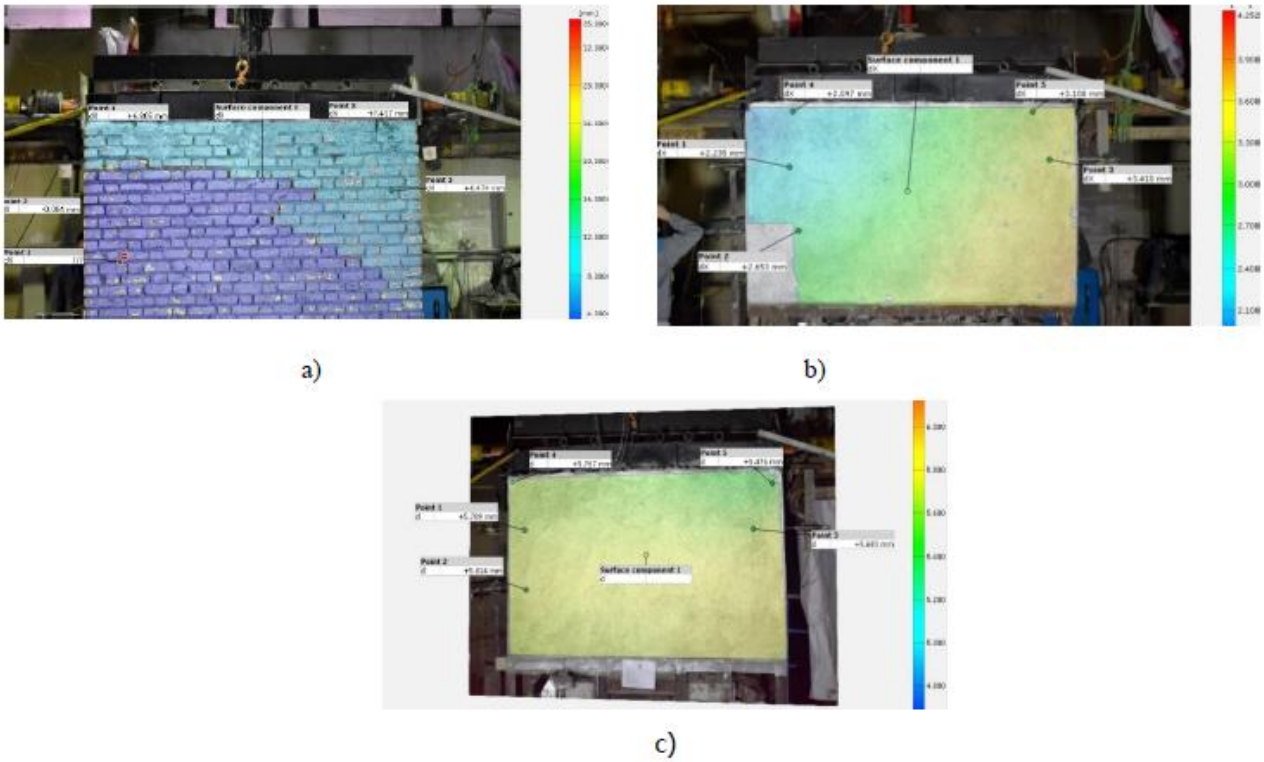

Fig. 13. Plots contour of full-field lateral displacement at peak load for samples (a) URM, (b) Re1-15, and (c) R1-15.

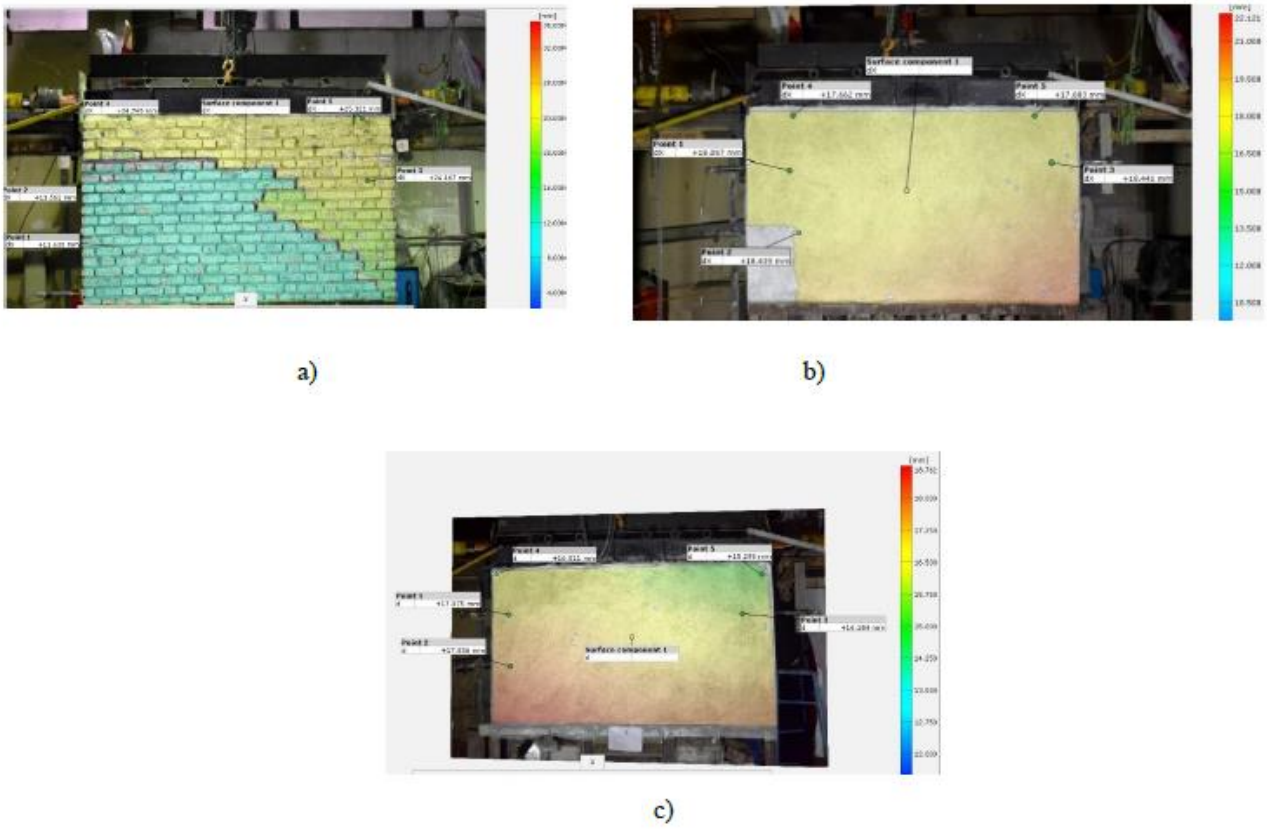

Fig. 14. Plots of contour of full-field lateral displacement at ultimate state for sample (a) URM; (b) Re1-15, and (c) R1-15.

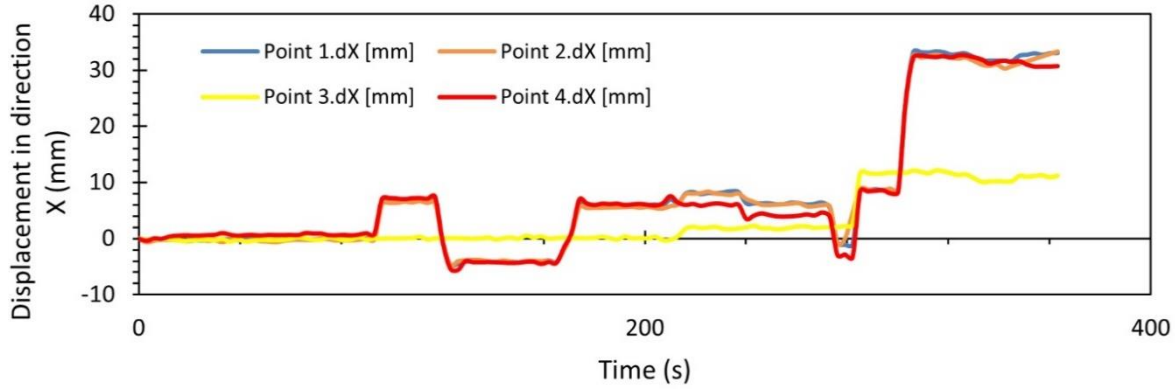

a)

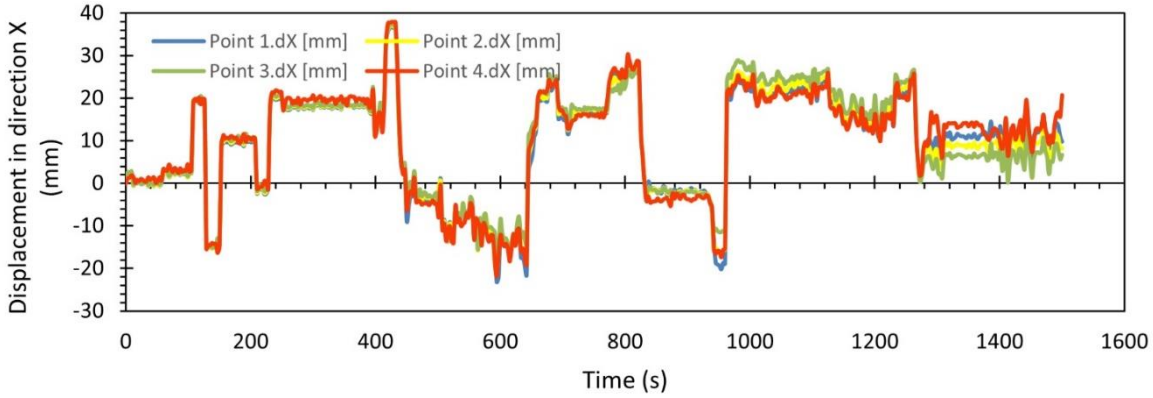

b)

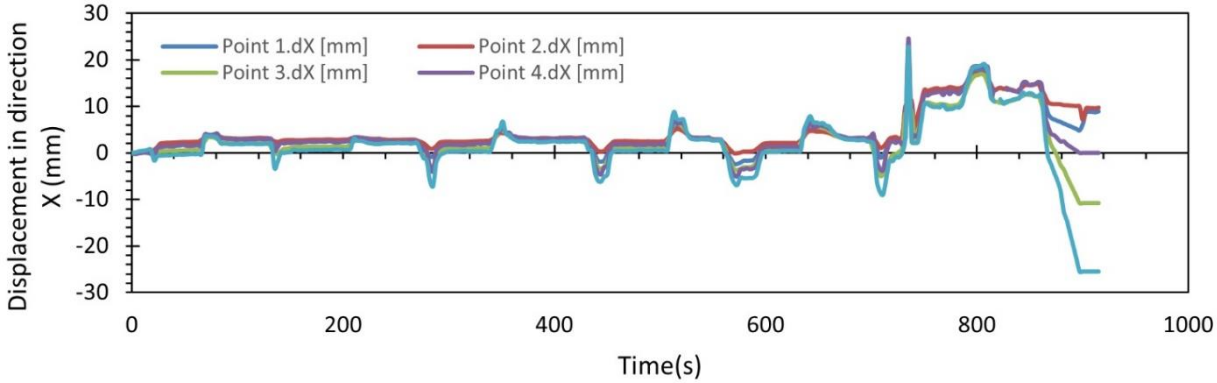

c)

Fig. 15. DIC test results: a) URM, b) Re1-15, c) R1-15.

3.9. Comparative analysis with existing studies

The experimental results confirm that GTRM strengthening effectively improves masonry walls' shear resistance, deformation capacity, and reduces the risk of brittle failure. Walls with fiber-reinforced mortar and GTRM mesh showed higher shear strength and strain than those with cement mortars, making fiber-reinforced mortars a suitable option for historic masonry due to their compatible pore structure and water absorption. As shown in Table 7 , TRM strengthening—both for repair and retrofitting—significantly enhances ductility, shear strength, and energy dissipation, with findings supported by experiments.

Table 6. literature overview on static cyclic response tests on GTRM-strengthened URM walls.

Specimens	Brick				Cement Mortar			Overlay Mortar			Tensile properties								Others				
																			Push	Pull	Push	Pull	
Masonry	Compressive strength of brick (MPa)	Three-point bending of clay brick (MPa)	Thickness (mm)	Thickness (mm)	The compressive strength of mortar (MPa)	The Tensile strength of mortar (MPa)	Thickness (mm)	The compressive strength of mortar (MPa)	The Tensile strength of mortar (MPa)	No. of Strengthened Sides	Mesh Type (Composite)	Number of Layers	Mesh Gride (mm)	Equivalent Diameter (mm)	The tensile strength (MPa)	Strengthening	L/H	Failure Mechanism	Ratio the Ductility of TRM to the unreinforced masonry Ductility.		Ratio the Peak load of TRM To the unreinforced masonry		Reference
solid brick	17.99	2.44	46	15	2.58	0.57	10	12.95	3.51	1	Basalt	1	17	0.032	1049	Re	1.00	D	1.48	1.48	1.20	0.91	[46]
solid brick	17.99	2.44	46	15	2.58	0.57	10	12.95	3.51	1	Basalt	1	17	0.032	1049	Re	1.00	D	1.50	1.50	1.11	1.01	[46]
solid brick	17.99	2.44	46	15	2.58	0.57	10	12.95	3.51	1	Basalt	1	17	0.032	1049	R	1.00	D	1.20	1.20	1.37	1.11	[46]
solid brick	17.99	2.44	46	15	2.58	0.57	10	12.95	3.51	1	Basalt	1	17	0.032	1049	R	1.00	D	1.47	1.47	1.30	1.50	[46]
solid brick	15.00	3.80	55	_	7.50	1.90	14	18.80	4.30	1	Glass	1	25	_	1276	Re	1.50	D	3.44	0.90	2.21	2.64	[47]
solid brick	15.00	3.80	55	_	7.50	1.90	14	18.80	4.30	1	Glass	1	25	_	1276	R	1.50	D	3.25	0.46	2.86	1.94	[47]
solid brick	27.93	4.37	50	_	4.68	1.65	20	4.68	1.65	1	Hemp	1	18	0.07	521	R	0.90	D	0.76	1.03	3.21	3.86	[32]
solid brick	27.93	4.37	50	_	4.68	1.65	20	4.68	1.65	1	Cotton	1	24	0.21	92	R	0.90	D	0.72	0.85	3.61	4.00	[32]
solid brick	27.93	4.37	50	_	4.68	1.65	20	4.68	1.65	1	Glass	1	22	0.04	674	R	0.90	D	0.78	0.85	3.24	3.65	[32]
solid brick	8.70	4.60	57	16	9.60	0.20	15	16.50	4.60	1	Glass	1	5	0.46	995	Re	1.67	S	1.10	0.94	1.75	1.32	Present Study
solid brick	8.70	4.60	57	16	9.60	0.20	15	16.50	4.60	1	Glass	1	5	0.46	995	R	1.67	S	0.77	0.53	2.81	2.55	Present Study

Re: repair

R: retrofit

D: diagonal stair- stepped cracking

S: shear sliding

4. Numerical modeling

This study used ABAQUS to create 3D finite element models of masonry walls via a simplified micro-modeling approach for behavioral simulation and parametric analyses. The models replicated wall geometry, embedding cohesive elements at mortar joints and within bricks to simulate crack initiation and propagation while ensuring deformation compatibility. Brick units were modeled with four-noded quadratic plane stress elements (Q8MEM, 205 mm thick), and mortar joints and potential cracks with four-noded linear interface elements (L8IF). Zero-thickness interface elements were used for joints and interfaces, requiring brick units to be slightly enlarged to maintain accurate wall geometry.

4.1. Numerical analysis

All elastic and plastic material properties used in the numerical modeling were derived from experimental tests and integrated into a masonry model replicating the tested specimens. Due to the brittle behavior of masonry and interaction effects, the Concrete Damage Plasticity (CDP) model was employed within ABAQUS [20] to realistically simulate tensile cracking and compressive crushing, including stiffness degradation under cyclic loading based on strength thresholds. To capture complex failure mechanisms such as splitting and toe crushing, embedded zero-thickness cohesive interface elements were added to represent potential crack paths. This combined CDP and cohesive surface approach significantly improves the accuracy and realism of crack propagation modeling in masonry structures. The CDP model is well-established for effectively simulating the nonlinear behavior of brittle materials like masonry units. Figure 17 illustrates the concrete response under axial compression and tension as represented by the CDP model. Figure 17-a depicts the stress-strain curve for concrete under tension, where the material initially exhibits linear elastic behavior until reaching the ultimate tensile stress, σtu. At this point, microcracking initiates as the material approaches failure. The subsequent softening of the curve reflects the propagation and localization of these microcracks within the concrete. Figure 17-b shows the stress-strain relationship for concrete under uniaxial compression. The concrete behaves linearly elastic up to the yield stress, σco. Upon reaching the ultimate compressive stress, σcu, the material undergoes gradual strain softening, indicative of its response to further deformation [48].

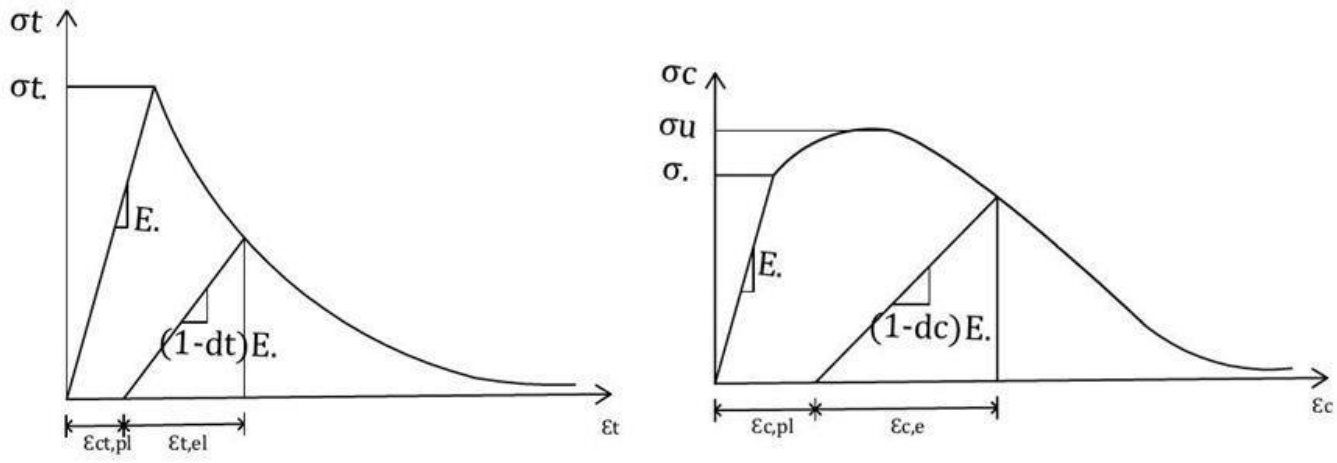

a) b)

Fig. 16.The tensile and compressive response of concrete to uniaxial loading described by Duval [20]. (a) Tension. (b) Compression**.**

4.2. Model Input

The masonry units were simulated using the material characteristics outlined in Table 8. Key parameters—including mass density, Young's modulus, viscosity coefficient (μ), and dilation angle (ψ)—were sourced either from experimental findings in this study or from earlier published work. Other variables, such as eccentricity, the biaxial-to-uniaxial compressive stress ratio (fbo/fco), and the stress invariant ratio (K) between tensile and compressive meridians, were adopted from existing literature.

In the CDP model, the compressive and tensile response parameters for both masonry and reinforcement materials were determined through experimental testing. As outlined in the Abaqus Theory Manual [20], tensile behavior must be defined from the peak stress point onward to account for softening, while compressive properties require characterization starting at the elastic limit and continuing through the post-yield softening phase [20].

Table 7. Mechanical characteristics of the masonry construction.

samples	Mass density (kg/m^3)	Young'smodulus (GPa)	μ	ψ	Eccentricity	Fbo/fco	K
Masonry prism	1850	2.8	0.001	10	0.1	1.16	0.67
Overlay mortar with fiber	1840	15.0	0.001	10	0.1	1.16	0.67
Overlay mortar without fiber	1820	15.0	0.001	10	0.1	1.16	0.67

4.3. Loading and boundary conditions

The specimens were tested under cyclic in-plane loading. First, a compressive axial load—simulating gravitational forces—was applied and kept constant during the analysis. Horizontal displacement was then introduced at the top of the walls until failure was observed. In the parametric analysis, axial stresses were considered for walls featuring fixed boundary conditions at their ends. For actual structural masonry buildings, walls generally have fixed supports at the base and remain unrestrained at the top.

4.4. Validation of model against experimental test results

Figure 18 compares the experimental envelope curves (push direction) with numerical load-displacement outcomes. The results demonstrate that the numerical analysis effectively replicates critical behavioral traits and aligns closely with the experimental load-displacement trends. To address material variability, the tensile properties of the TRM coatings in models URM and R1-15 were calibrated to ensure consistency between simulated and experimentally observed failure modes. Table 9 summarizes the comparison between finite element predictions and experimental measurements, emphasizing key metrics such as maximum load capacity and the displacement corresponding to an 80% reduction in lateral strength post-peak. The data confirm that the finite element models reliably predict the specimens' ultimate resistance, validating their accuracy in simulating structural behavior.

Table 8. Comparison of the experimental and FE results' displacement and lateral strength.

Specimen	$P_{max,EXP}$ (kN)	$P_{max,FE}$ (kN)	$P_{max,EXP}/P_{max,FE}$	$\Delta_{u,EXP}$ (m)	$\Delta_{u,FE}$ (m)	$\Delta_{u,EXP}/\Delta_{u,FE}$
URM	36.50	38.31	0.95	0.010	0.008	1.25
R1-15	100.34	112.10	0.90	0.030	0.025	1.20

$P_{max,EXP}$: the experimental peak load in the push direction

$P_{max,FE}$:the numerical peak load

$\Delta_{u,EXP}$:the experimental displacement in the push direction at failure

$\Delta_{u,FE}$: the numerical displacement at failure

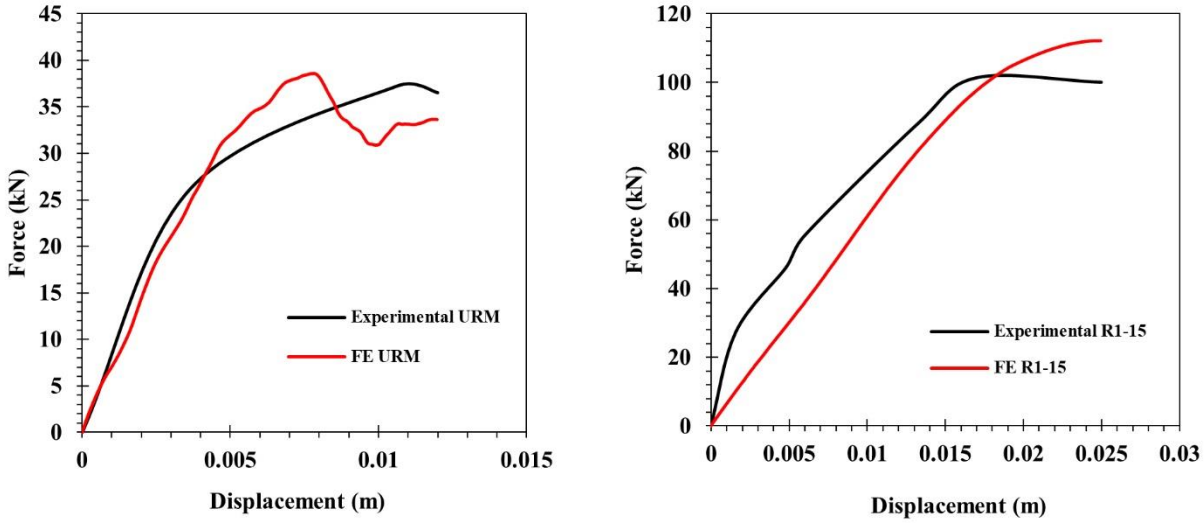

Figure 17: Comparing the push-direction envelopecurves taken from the experimental data with the lateral load-displacement curves derived from the FE analysis.

4.5.1. Parametric study

The validated finite element wall model was used to investigate the effects of layer thickness, number of reinforcement layers, vertical pre-compression levels, and mortar type on the in-plane behavior of unreinforced masonry (URM) walls. Material properties for all simulations are listed in Table 10. Specimens were systematically labeled based on their geometry and loading conditions. The study's results highlight how these variables influence crack propagation and load-displacement responses. These parametric findings directly inform masonry retrofit design by identifying key performance factors, quantifying improvements, and validating the models against experimental data and design codes. Consequently, the outcomes assist engineers in making informed decisions regarding material selection, reinforcement detailing, and realistic performance expectations for TRM-strengthened masonry in both repair and retrofit applications.

Table 9. The material properties for all models.

Group	Model ID	σ_0 MPa	t_{matrix} mm	Layer mesh	overlay mortar
Aa	Aa1	0.0	30.0	1	MF
	Aa2		22.5		
	Aa3		15.0		
Ab	Ab1	0.1	30.0		
	Ab2		22.5		
	Ab3		15.0		
Ac	Ac1	0.2	30.0		
	Ac2		22.5		
	Ac3		15.0		
Ad	Ad1	0.0	30.0		
	Ad2		22.5		
	Ad3		15.0		
Ae	Ae1	0.1	30.0	2	
	Ae2		22.5		
	Ae3		15.0		
Af	Af1	0.2	30.0		
	Af2		22.5		
	Af3		15.0		
Ag	Ag1	0.0	30.0		
	Ag2		22.5		

	Ag3		15.0		
	Ah1		30.0		
Ah	Ah2	0.1	22.5	3	
	Ah3		15.0		
	Ai1		30.0		
Ai	Ai2	0.2	22.5		
	Ai3		15.0		
	Ba1		30.0		
Ba	Ba2	0.0	22.5		
	Ba3		15.0		
	Bb1		30.0		
Bb	Bb2	0.1	22.5		
	Bb3		15.0	1	
	Bc1		30.0		
Bc	Bc2	0.2	22.5		
	Bc3		15.0		
	Bd1		30.0		
Bd	Bd2	0.0	22.5		
	Bd3		15.0		
	Be1		30.0		
Be	Be2	0.1	22.5		
	Be3		15.0		
	Bf1		30.0	2	
Bf	Bf2	0.2	22.5		
	Bf3		15.0		
	Bg1		30.0		
Bg	Bg2	0.0	22.5		MW
	Bg3		15.0		
	Bh1		30.0		
Bh	Bh2	0.1	22.5		
	Bh3		15.0		
	Bi1		30.0	3	
Bi	Bi2	0.2	22.5		
	Bi3		15.0		

σ_0: pre-compression stress, t_{matrix}: thickness of overlay mortar

4.5.1.1. The mechanical parameters' ranges of variability

The mechanical properties applied in the parametric study are compiled in Table 10, encompassing data from 54 reinforced wall specimens. Each model isolates a single critical variable for analysis. Since vertical compression plays a critical role in the in-plane shear response of masonry walls, compressive stress levels of 0.0 MPa, 0.1 MPa, and 0.2 MPa were adopted to reflect common actual conditions in existing masonry buildings.

4.5.1.2. Pre-compression stress variation

Numerical simulations demonstrated that the lateral load-bearing capacity and failure mechanisms of URM walls depend significantly on pre-compression stress levels, which vary based on a wall's location within a structure. Historical seismic events have revealed differences in failure patterns among walls subjected to in-plane loading across different floors of the same building. In Iran, where URM buildings are typically low-rise, a pre-compression stress of 0.2 MPa is regarded as comparatively high [49]. However, research in the Middle East has investigated even greater compressive stress levels to gain deeper insights into masonry wall behavior under shear forces. To align with both regional architectural practices and broader experimental frameworks, this study evaluates pre-compression stresses of 0.0 MPa, 0.1 MPa, and 0.2 MPa in its parametric analysis.

3.2.1.3. Plaster thickness (refitted masonry)

This section investigates how plaster thickness influences structural response. Three numerical models were simulated with plaster layers measuring 15.0 mm, 22.5 mm, and 30.0 mm in thickness. Material properties,

interface behavior, loading protocols, and mesh configurations mirrored the parameters outlined in Section 3 to ensure consistency across the analyses.

4.5.1.4. Number of TRM layers

Enhancing structural capacity in masonry systems typically requires adding more TRM layers. However, simply increasing the number of TRM layers does not always translate to improved mechanical performance. Suboptimal bonding at the interface can disrupt stress transfer between layers [50], preventing full utilization of the textile reinforcement's strength. Such bonding deficiencies often result in early detachment from the substrate and diminished system ductility [9],[6,47,51–55].

4.5.1.5. Overlay mortar

This study analyzes the structural influence of two mortar types: fiber-reinforced mortar (MF) and non-fiber (plain) mortar (MW).

4.6. Discussion and results

This section details and evaluates the outcomes for the 54 reinforced walls and URM models. The numerical load-displacement relationships are plotted and subsequently converted into simplified bilinear curves to facilitate data interpretation. Additionally, the damage progression in the walls is analyzed by comparing stiffness and ductility ratios, enabling a comprehensive evaluation of structural performance under the diverse loading scenarios investigated in this research.

While the analysis confirms that thicker and multi-layered TRM overlays can enhance the lateral load resistance of retrofitted masonry, the effectiveness of the intervention fundamentally depends on the quality of bond at the TRM–masonry interface. This interface governs stress transfer from the masonry substrate to the retrofit layer and strongly influences the activation and ultimate performance of the reinforcement. Poor bonding, often caused by inadequate surface preparation or material incompatibility, can lead to premature debonding, reduced ductility, and limited strength enhancement, even with nominally optimal overlay thickness. Future research should explicitly account for interface behavior in both experimental and numerical assessments, and practitioners are encouraged to carefully control adhesion conditions during TRM installation for best results [5].

4.6.1. Stiffness

The outcomes for the 54 reinforced walls are compiled in Table 11, which includes data for all tested specimens. The Table 11 provides the following key parameters: Vmax is the peak lateral load (shear strength) under in-plane loading; δcr is the horizontal displacement at first significant cracking, determined from the envelope curve at 0.7Vmax; δmax is the displacement corresponding to the peak load (Vmax); δu is the ultimate displacement, defined as the endpoint of the envelope curve; K_{init} is the Initial stiffness, calculated as the secant stiffness of the envelope curve at 0.15Vmax ; K_{eff} is the Effective stiffness, derived as 0.7Vmax divided by δcr [56]; K_{eff}/K_{init}: Ratio quantifying the stiffness reduction after cracking.These parameters enable a systematic evaluation of stiffness degradation, cracking progression, and ductility across specimens under varying loading scenarios.

The K_{eff} / K_{init} ratios reported in Table 11 are consistent with Eurocode 8 – Part 3 [22] ,which advocates using cracked stiffness values for seismic assessments of masonry systems. When detailed evaluations of stiffness degradation are unavailable, the code proposes a default ratio of 0.5. This study's results align closely with this recommended value. Notably, while this simplified ratio is primarily intended for undamaged, unreinforced masonry walls, the data suggest it remains applicable to damaged structures and those retrofitted with TRM, demonstrating its broader relevance in seismic evaluations.

Table 10. Main numerical results obtained from envelope curves.

Model	V_{max} (kN)	V_u (kN)	V_u/V_{max}	δ_y (mm)	δ_{cr} (mm)	δ_u (mm)	δ_{max} (mm)	$\mu=\delta_u/\delta_y$	K_{initi} (kN/mm)	K_{eff} (kN/mm)	K_{eff}/K_{initi}	θcr (%)	θy (%)	θmax (%)	θu (%)
URM	35	34	0.97	6	4	13	32	2.00	7.80	5.30	0.68	0.30	0.40	0.50	0.80
Aa1	108	86	0.80	8	13	25	32	3.20	6.40	5.70	0.88	0.90	1.00	2.20	3.20
Aa2	107	97	0.91	17	14	50	29	2.86	6.50	5.50	0.86	0.90	1.20	1.90	3.30
Aa3	102	95	0.93	17	13	42	23	2.50	6.50	5.70	0.87	0.80	1.10	1.60	2.80
Ab1	133	107	0.80	19	17	50	36	2.63	6.50	5.60	0.86	1.10	1.30	2.40	3.30
Ab2	128	103	0.80	18	16	49	33	2.73	6.60	5.80	0.88	1.00	1.20	2.20	3.20
Ab3	125	100	0.80	17	15	49	25	2.84	6.60	5.80	0.89	1.00	1.10	1.60	3.20
Ac1	168	135	0.80	24	21	65	38	2.75	6.60	5.70	0.87	1.40	1.60	2.50	4.30
Ac2	164	132	0.80	8	20	23	35	3.06	6.50	5.80	0.9	1.30	2.30	2.50	4.60
Ac3	160	158	0.98	27	20	69	38	2.52	6.60	5.80	0.87	1.30	1.80	2.50	4.60
Ad1	146	142	0.97	26	19	60	41	2.31	6.60	5.30	0.8	1.30	1.80	2.70	4.10
Ad2	137	109	0.80	20	18	60	38	2.95	6.60	5.40	0.82	1.20	1.40	2.50	4.00
Ad3	134	119	0.89	22	17	60	35	2.75	6.60	5.50	0.83	1.10	1.50	2.30	4.00
Ae1	161	160	0.99	30	21	62	45	2.06	6.50	5.30	0.82	1.40	2.00	3.00	4.10
Ae2	154	154	1.00	27	19	60	39	2.19	6.60	5.60	0.85	1.30	1.80	2.60	4.00
Ae3	147	139	0.94	25	18	62	40	2.50	6.50	5.60	0.86	1.20	1.70	2.70	4.10
Af1	206	201	0.97	37	27	81	64	2.19	6.60	5.40	0.82	1.80	2.50	4.30	5.40
Af2	198	185	0.93	34	25	82	47	2.43	6.60	5.50	0.83	1.70	2.30	3.20	5.50
Af3	192	186	0.97	34	24	80	47	2.37	6.70	5.50	0.83	1.60	2.30	3.10	5.30
Ag1	200	186	0.93	35	27	88	67	2.48	6.60	5.30	0.79	1.80	2.40	4.40	5.90
Ag2	195	175	0.90	32	25	89	48	2.76	6.50	5.40	0.84	1.70	2.20	3.20	5.90
Ag3	191	190	0.99	35	24	76	49	2.18	6.50	5.40	0.84	1.60	2.30	3.20	5.10
Ah1	223	212	0.95	39	29	100	68	2.58	6.60	5.50	0.83	1.90	2.60	4.60	6.70
Ah2	200	160	0.80	30	26	100	47	3.32	6.60	5.30	0.8	1.80	2.00	3.10	6.70
Ah3	203	201	0.99	36	25	90	47	2.47	6.60	5.50	0.84	1.70	2.40	3.10	6.00
Ai1	232	220	0.95	40	30	100	80	2.52	6.70	5.50	0.82	2.00	2.70	5.20	6.70
Ai2	222	201	0.90	36	29	100	64	2.74	6.60	5.50	0.84	1.90	2.40	4.30	6.70
Ai3	222	205	0.92	37	28	100	67	2.67	6.60	5.50	0.84	1.90	2.50	4.50	6.70
Ba1	110	104	0.94	19	14	40	41	2.43	6.50	5.40	0.84	1.00	1.10	2.70	2.60
Ba2	106	96	0.91	17	13	40	26	2.32	6.50	5.60	0.86	0.90	1.20	1.70	2.70
Ba3	102	98	0.96	17	12	41	22	2.38	6.50	5.70	0.87	0.80	1.10	1.50	2.70
Bb1	131	125	0.96	22	17	42	33	2.00	6.60	5.60	0.86	1.10	1.50	2.20	2.80
Bb2	133	121	0.91	21	16	49	33	2.30	6.60	5.80	0.88	1.10	1.40	2.20	3.20
Bb3	138	128	0.93	23	16	50	36	2.20	6.60	5.70	0.86	1.10	1.50	2.40	3.30
Bc1	151	140	0.93	25	19	58	34	2.34	6.30	5.70	0.86	1.20	1.70	2.30	3.90
Bc2	144	135	0.94	23	17	56	36	2.89	6.60	5.80	0.92	1.20	1.60	2.40	3.70
Bc3	148	139	0.94	24	17	52	36	2.21	6.50	5.90	0.9	1.20	1.60	2.40	3.50
Bd1	125	114	0.91	20	16	52	34	2.56	6.50	5.60	0.86	1.00	1.40	2.20	3.50
Bd2	121	111	0.92	19	14	52	35	2.97	6.30	5.90	0.93	0.90	1.30	2.30	3.50
Bd3	112	106	0.94	18	13	52	35	2.89	6.60	5.90	0.89	0. 9	1.20	2.30	3.50
Be1	154	148	0.96	27	20	68	42	2.51	6.60	5.50	0.83	1.30	1.80	2.80	4.50
Be2	151	142	0.94	25	19	60	37	2.19	6.60	5.60	0.86	1.30	1.80	2.50	4.00
Be3	152	139	0.92	24	18	60	43	2.50	6.60	5.80	0.87	1.20	1.60	2.70	4.00
Bf1	171	162	0.95	30	22	68	43	2.30	6.50	5.50	0.84	1.50	2.00	2.90	4.50
Bf2	160	151	0.95	28	20	68	39	2.49	6.60	5.30	0.81	1.30	1.80	2.60	4.50
Bf3	169	158	0.94	29	21	60	43	2.10	6.60	5.50	0.84	1.40	1.90	2.80	4.00
Bg1	187	175	0.94	33	25	92	49	2.58	6.50	5.30	0.8	1.70	2.40	3.30	6.10
Bg2	182	168	0.92	31	23	77	50	2.49	6.50	5.50	0.84	1.50	2.00	3.30	5.10
Bg3	187	175	0.94	32	23	74	50	2.10	6.50	5.50	0.84	1.60	2.40	3.30	4.90
Bh1	197	185	0.94	35	26	110	68	3.15	6.50	5.30	0.81	1.70	2.30	4.50	7.30
Bh2	189	174	0.92	31	24	88	44	2.80	6.60	5.50	0.84	1.50	2.10	2.90	5.90
Bh3	199	187	0.94	34	25	81	47	2.40	6.60	5.50	0.84	1.60	2.20	3.20	5.40
Bi1	215	210	0.98	40	29	105	72	2.54	6.50	5.30	0.81	1.90	2.70	4.80	6.70
Bi2	197	191	0.97	34	26	101	49	2.93	6.50	5.60	0.86	1.60	2.40	3.30	7.00
Bi3	209	196	0.94	35	25	95	47	2.58	6.60	5.60	0.84	1.70	2.50	3.10	6.30

4.6.2. Bilinear idealization and ductility ratio

Table 11 summarizes the simplified bilinear load-displacement relationships for the 54 reinforced walls and the URM models analyzed earlier. The results clearly demonstrate that the TRM reinforcement improves effective stiffness in all strengthened cases, underscoring its role in mitigating crack propagation in masonry under in-plane cyclic loading. Furthermore, the initial stiffness (slope of the first segment) of the bilinear curves remains nearly identical across all 54 reinforced specimens, indicating uniformity in the elastic response of the retrofitted systems.

Eurocode 8 – Part 3 [22] establishes two critical drift thresholds for seismic assessment of masonry buildings, including unreinforced walls under shear loading. The Significant Damage (SD) limit state corresponds to a drift of 0.004, while the Near Collapse (NC) limit state occurs at a drift of 0.0053 (equivalent to 4/3 of the SD value). As shown in Table 11, these thresholds align with the δmax (displacement at peak load) and δu (ultimate displacement) values derived from the numerical load-displacement curves [57,58] .The findings demonstrate that the code's safety limits are suitable for both unreinforced and TRM-strengthened walls under evaluation. However, failure modes such as rocking and toe crushing caused drifts to exceed these thresholds during testing. These trends mirror observations from previous research on both brick [46] and stone [59] masonry walls, highlighting the broader relevance of such mechanisms in seismic performance analyses.

The evolution of damage and cracking patterns observed during testing served as primary indicators for identifying distinct damage levels in the masonry walls. These damage levels are mapped to specific inflection points on the experimental force-displacement curves generated during testing. Categorizing these damage states improves the assessment of masonry wall behavior under seismic forces and supports the definition of performance thresholds for retrofit design. As outlined in studies [57,59] four limit states are typically categorized using displacement and drift criteria:

- Drift at cracking (θcr): This is the drift at which the first cracks appear in the masonry. Although these cracks may not always be visible to the naked eye, they are indicated by a change in slope on the envelope curve. In this study, θcr corresponds to the displacement at which the load reaches 70% of the peak force (Vmax).
- Drift at yielding (θy): Defined through the bilinear approximation of the force-displacement curve, this drift corresponds to the ultimate load (Vu).
- Drift at maximum force (θmax): Measured at the peak load, this drift marks the beginning of concentrated damage in a few cracks and aligns with the Significant Damage (SD) limit state specified in design codes.
- Ultimate drift (θu): This drift corresponds to a 20% reduction in lateral strength from the peak load and is associated with the Near Collapse (NC) limit state defined by the codes.

Walls that exhibited flexural or rocking failure mechanisms demonstrated significantly higher ultimate drift values (θu), averaging above 0.8%.

The application of TRM led to substantial quantitative improvements in seismic performance indicators for both repaired (Re1-15) and retrofitted (R1-15) wall specimens. Specifically, the Re1-15 wall achieved a peak lateral strength 180% that of the unreinforced reference, with a fivefold increase in ductility and a 35% greater ultimate drift. The R1-15 retrofitted specimen further increased peak load by 230% and final drift by 20% compared to the control. Overall, TRM overlays resulted in up to 4.8 times greater shear strength, as well as enhanced displacement and energy dissipation capacities. These results confirm that TRM systems provide significant and quantifiable improvements in the seismic resilience of existing masonry walls. Numerical drift values corresponding to different damage levels are shown in Table 11.

4.6.3. Comparison of different groups

In contrast, Figure 19 (a and b) presents the maximum lateral load resistance (Vmax) for each of the 54 reinforced walls, grouped by pre-compression level, number of TRM layers, and mortar overlay thickness. The findings reveal that lateral load capacity improves with greater mortar thickness and additional TRM layers, with this enhancement being most notable in specimen Ai1.

Therefore, the increased load capacity observed in groups Ag to Ai and Bg to Bi is likely related to the combined effects of increased number of TRM layers and increased matrix thickness. In comparision with Ai1 and Bi1, the maximum shear force is increased by 8% that due to have fiber in overlay mortar.

Figure 19-b further demonstrates that decreasing wall layer thickness, TRM layer count, vertical pre-compression stress, or altering TRM mortar type causes only a minor reduction in lateral load capacity across the investigated parameter ranges. This indicates that lateral load capacity exhibits moderate sensitivity to changes in these variables.

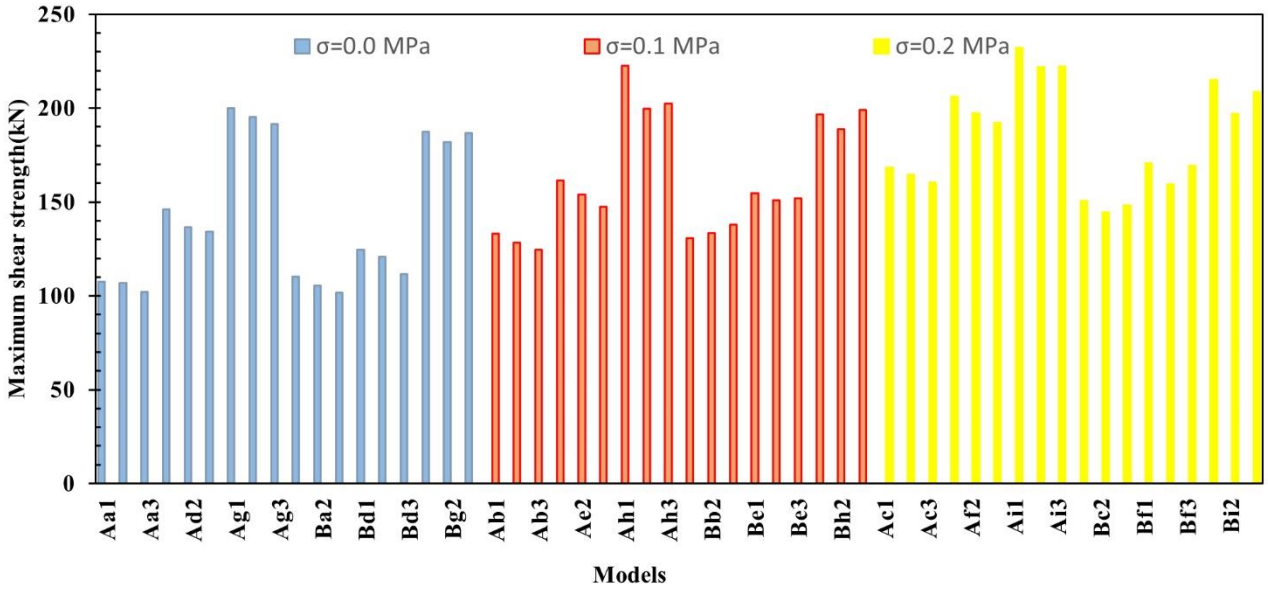

a)

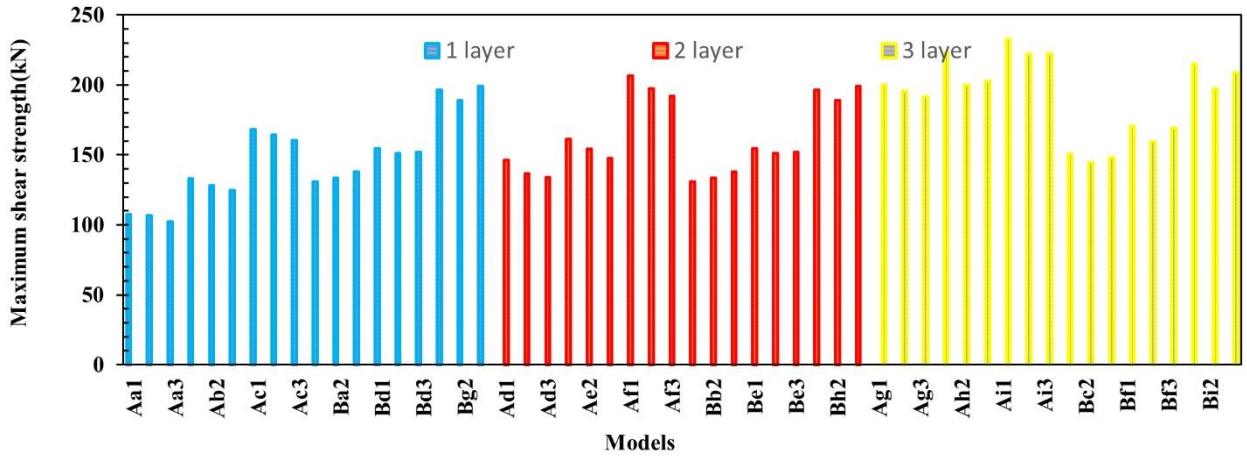

b)

Fig. 18. Maximum shear strength for different configurations: a) σ =0 ,0.1, and 0.2 b) 1 layer to 3 layer.

4.6.4. Failure mode specifications

The numerical analysis of masonry walls strengthened with Textile-Reinforced Mortar (TRM), considering rocking failure mode and toe crushing (as outlined in Table 11), shows that the reinforced walls maintain a rocking failure mode similar to that of unreinforced walls. However, the presence of the TRM mortar enhances the overall wall integrity, resulting in more ductile behavior demonstrated by a positively sloped force-displacement curve. Crack patterns resemble those of unreinforced walls but with a slightly larger crack size on the wall sides due to the improved structural cohesion provided by the TRM layer. Figure 20 displays these results, including plastic strain contours in the TRM, which reveal nonlinear behavior across most of the wall except in the toe region.

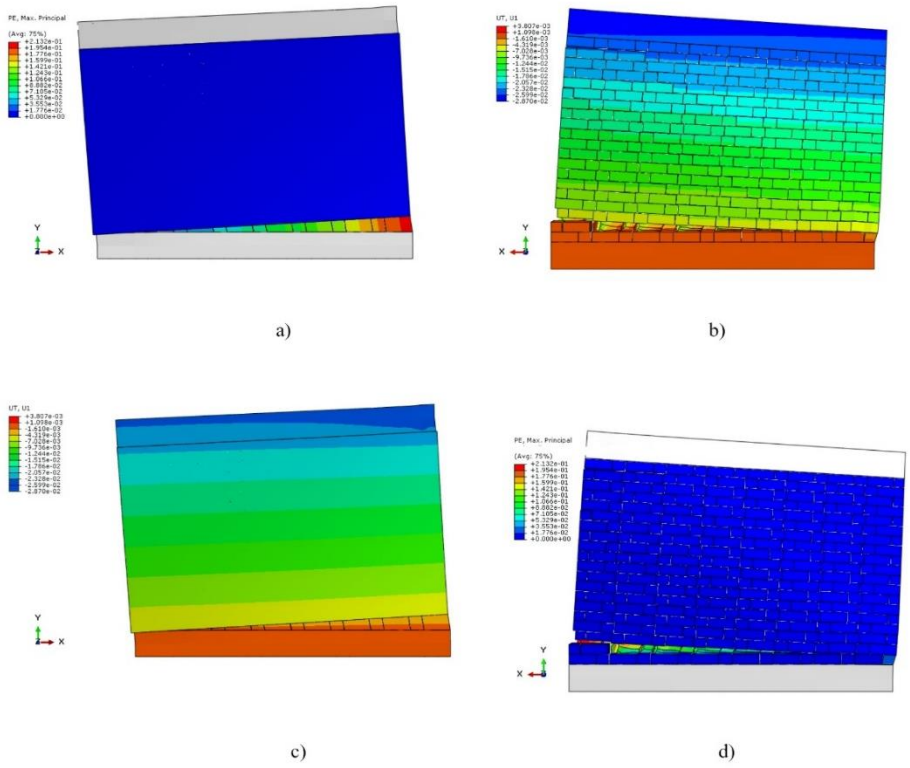

Fig. 19. Countor plot in Ba3, a) Failure mode of numerical wall of front view, b) Failure mode of numerical wall of back view, c) Maximum princepal plastic strain distrubition in front view, and d) Maximum princepal platic strain distrubition in back view.

4.7. Validation of model against experimental test results

4.7.1. Load-displacement response

Figure 21 compares the lateral load-displacement envelope curves from experimental tests with the FEA simulations for the URM, Ai, and Bi wall groups. The results show strong alignment between experimental and numerical data, particularly in the elastic stiffness of the URM walls. Given the symmetrical design of the tested walls, FEA simulations were performed for unidirectional loading, with the assumption of symmetrical behavior in both positive and negative directions to enable comparison with full experimental curves. The FEA outcomes closely match experimental trends, accurately replicating the nonlinear response after the initial linear phase. However, the simulations slightly overpredict peak lateral loads compared to experimental values. This divergence is attributed to the monotonic displacement protocol used in FEA, contrasting with the cyclic loading applied in physical tests. Despite this, the discrepancy in maximum load between FEA and URM experiments remained below 10%. The models also predicted higher initial stiffness values than those observed experimentally, with wall Ai1 exhibiting notably greater FEA-derived stiffness compared to Bi1.

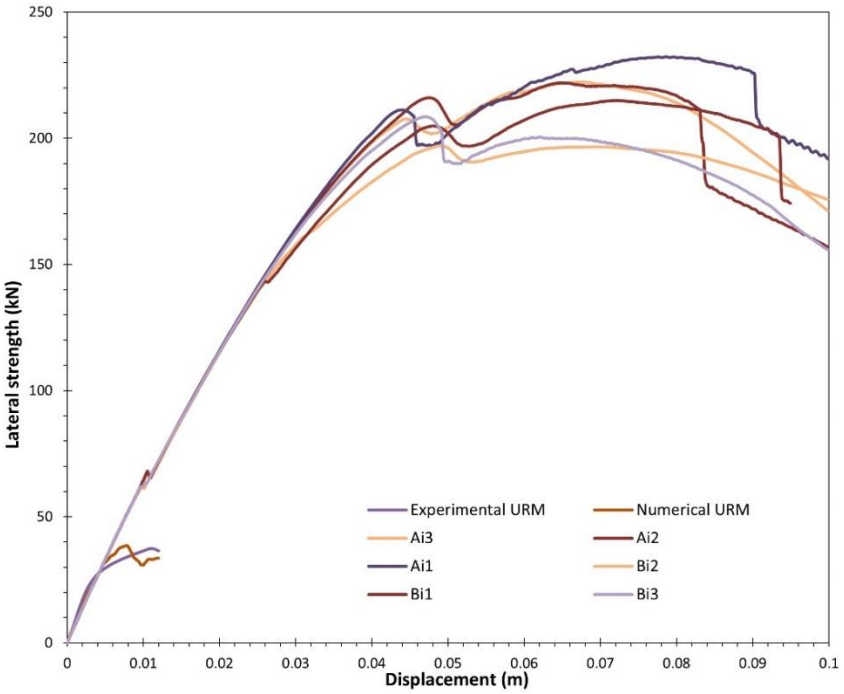

Fig. 20. lateral strength-displacement curve of models in groups of Ai and Bi.

4.8. Existing analytical models

The contribution of TRM systems to the in-plane shear capacity of masonry walls can be assessed using the analytical methods outlined in ACI 549.4R-20 [15], CNR DT 215 2018 [16] , and Eurocode 8 (EC8) Part 3 [22], as summarized in Table 12. These approaches assume that the total shear capacity (V_{Rd}) of a retrofitted masonry wall is the sum of the masonry's inherent shear capacity (V_m) and the additional shear capacity provided by the TRM strengthening system (V_{TRM}).

Table 11. The role composite materials and unreinforced masonry in shear strength based on to analytical approaches.

V_m	V_{TRM}	V_{Rd}	Model
$min\left(V_{ss}, V_{sf}, V_{dt}, V_c\right)$	$S \times n \times A_f \times L_f \times f_v$	$V_m + V_{TRM}$	ACI 549.4R-20 [15]
$V_t = H \times t \times (\frac{1.5\tau_{0d}}{P}) \times \sqrt{(1 + (\frac{\sigma_0}{1.5 \times \tau_{0d}}))}$	$0.5 \times n_f \times t_{vf} \times l_f \times a_f \times \varepsilon_{fd} \times E_f$	$V_m + V_{TRM}$	CNR2018 [16]
$min\left(V_{sf}, V_{dt}, V_t\right)$	$0.9 \times d \times \rho_f \times E_f \times t_f \times \varepsilon_f$	$V_m + V_{TRM}$	EC8 part 3 [22]

ACI 549.4R-20 : [31]

shear friction: $V_{sf} = \frac{\tau_{0m} \times A_n}{1 - \mu_{0m} \times tan\,\theta}$, diagonal tension: $V_{dt} = tan\,\theta + \frac{\sqrt{21.16 - tan\,\theta^2}}{10.58} \times f_t \times A_n$, toe crushing: $Vc = \frac{2w \times f'_m}{3h + 2w \times tan\,\theta}$

CNR 2013: [27]

shear capacity: $V_{RD,max} = 0.3 \times {f_{md}}^h \times t \times l$

τ_{0d}: strength of mortar joint bond

ρ_f and b_f: respectively the spacing and width of TRM application

P: coefficient factor of the stresses, equal to the maximum value 1.5

A_n: net cross-sectional area of the URM

τ_{0m}: modified strength of shear bond of mortar joint

μ_{om}: modified internal shear friction coefficient in mortar joint

f_{vd}: design masonry shear strength

n: layers of mesh reinforcement

S: number of side reinforcement

t_{vf}: equivalent thickness of a network layer with parallel fibers to the shear force

t: wall thickness

γ_{Rd}: Partial factor of the TRM system

γ_m: Partial factor of the masonry

E_f: tensile modulus of elasticity of textile

ε_{ffd}: debonding strain of textile

ε_{fd}: TRM design deformation

ε_{fm}: transition point of strengthening mortar strain

f_{vd}: shear strength of design masonry

a_l: (value 0.8) coefficient including the decreased extensional resistance of the fibers exposed to shear stress

4.8.1. Comparing parametric analyses to current analytical models

After confirming the accuracy of the FEM through comparisons with theoretical predictions and code-based formulations, this study narrows its focus to squat walls to specifically investigate rocking failure modes. Consequently, the following geometric parameters are held constant across all analyses: H = 1500 mm, L = 2500 mm, s = 205 mm, slenderness λ = H/L = 0.6.All walls are modeled as cantilevered, fixed at one end to replicate typical masonry boundary conditions (see (Figure 2)).

This section examines the differences between analytical and numerical results by comparing the shear strengths predicted by the analytical model (ACI 549.4R-20 [15]) with those obtained from the numerical simulations.

4.8.1.1. The numerical and the analytical results

Figure 22 compares theoretical shear resistance predictions with numerical results from finite element method (FEM) simulations for masonry walls. The theoretical values are generally slightly lower than numerical outcomes, showing modest discrepancies. Data points near the identity line (Vpred = Vnum) indicate strong agreement, while points above the line suggest conservative overestimations by theory, and points below indicate underestimations of actual capacity.

The modeling uses a homogenized approach capable of accurately simulating common masonry failure modes such as rocking and toe crushing, consistent with Eurocode 8 [22] and ACI 549.4R-20 [15], as well as previous research . Both numerical and theoretical models employ homogenized masonry representations, validating the comparison. On average, theoretical shear capacities are about 20% lower than numerical predictions, ensuring safe, conservative design.

This close correlation demonstrates the reliability of micro-modeling FEM techniques not only for diagonal shear failure typical in irregular masonry but also for regular masonry walls. The study's parametric results aid masonry retrofit design by identifying key parameters, quantifying performance gains, and validating against experiments and standards, helping engineers select materials, reinforcement details, and predict performance realistically.

The conservative nature of the models arises from simplifying assumptions and safety factors on material properties, failure modes, and bond behavior, to maintain safety and code compliance in practical design.

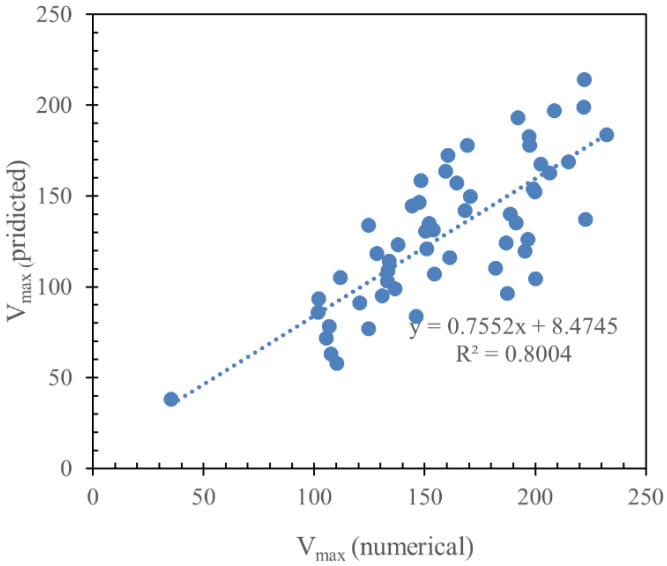

Fig. 21. Comparison between theoretical shear strength and numerical predictions for strengthened walls.

5.Discussion

This study demonstrated that Textile Reinforced Mortar (TRM) considerably enhances the in-plane cyclic performance of unreinforced masonry (URM) walls. Both experimental and numerical analyses confirmed that TRM can restore and significantly increase the load-bearing capacity of damaged walls, achieving peak load gains of up to 180% for repaired specimens and 230% for retrofitted specimens, while also improving stiffness, crack control, ductility, and energy dissipation [1–3]. Strengthened walls showed a transition from brittle shear sliding to a more ductile, composite failure mode, as confirmed by digital image correlation (DIC) analysis [1–3].

Finite element simulations, which closely matched experimental results, emphasized the importance of TRM layer thickness, reinforcement layers, and vertical pre-compression stress on wall performance [4]. These findings are in line with current design guidelines such as ACI 549.4R-20 [15], CNR DT 215 2018 [16], and Eurocode 8 (EC8) Part 3 [22].

The finite element model employed in this study utilized a simplified micro-modeling strategy, assuming fully bonded TRM–masonry interfaces and incorporating cohesive elements to simulate cracking behavior. Although widely adopted in the literature [60–62], such assumptions may lead to overestimation of load transfer and ductility, as they do not fully capture critical interface phenomena like debonding, slip, or delamination—especially under cyclic loading. The use of cohesive elements partially mitigates this by enabling localized damage modeling; however, their parameters remain idealized. To improve predictive accuracy, future studies should adopt experimentally calibrated interface models that reflect partial bonding and progressive degradation [42,63]. Practitioners should interpret the simulation results with an understanding of these modeling limitations.

Future research should explore how material properties, interface behavior, and reinforcement configurations influence the accuracy of numerical models for TRM-strengthened masonry walls. Sensitivity analyses and thorough validation against experimental and field data are crucial to improve simulation reliability. This work will help develop stronger, more practical design guidelines for real-world masonry retrofitting and repair.

While increasing the thickness of the TRM overlay generally improves the strength and ductility of masonry walls, the overall effectiveness strongly depends on the quality of the bond at the TRM–masonry interface. Poor bonding can lead to premature debonding or slippage, which diminishes the advantages of thicker

overlays or stronger meshes. Therefore, proper surface preparation and mortar compatibility are essential for optimal performance. Experimental results based on idealized interface conditions may overestimate actual field outcomes. Future research should focus on the variability of interface bonding and develop quality control standards to ensure reliable performance in practical applications.

Despite the promising results, practical challenges remain for real-world applications due to construction irregularities, material variability, surface preparation demands, quality control, anchorage detailing, and environmental factors (e.g., moisture, freeze–thaw cycles, and UV radiation), which may reduce long-term performance [50]. Achieving laboratory-level performance in the field requires proper planning, skilled supervision, and mock-up testing [50].

DIC proved effective for qualitative deformation and crack detection; however, future research should focus on quantitative strain and crack analyses by integrating DIC with LVDT measurements and finite element modeling. Advanced DIC-based indices could further improve predictive modeling [64].

Comparison with previous studies confirmed that G-TRM retrofitted and repaired walls achieved superior peak strength and drift capacity, with slight variations attributed to differences in wall geometry, experimental setup, and loading protocols [10,62,63] (Table 13).

Table 12. Comparison of key results with previous studies.

Study	TRM Type	Peak Load Increase (%)	Drift Capacity Increase (%)	Strengthening Approach
Present Study	G-TRM	180–230	20–35	One-side overlay, AR mesh
Triantafillou et al. [10]	G-TRM	175–210	18–28	Two-side overlay
Raouf & Jalal [62]	Steel/TRM	160–220	15–30	Repair after pre-damage
Babaei Darabad & Nanni [61]	Basalt TRM	120–180	15–25	One-side overlay

Overall, TRM is validated as a practical and cost-effective [65] seismic retrofitting solution for earthquake-prone regions. Future research should focus on full-scale and dynamic testing, advanced interface modeling, durability assessments, and development of standardized design guidelines [64].

6. Summary and conclusions

The article explores experimental research conducted on masonry walls, scaled down to 2/3 their original size, to investigate the impact of GTRM reinforcement on seismic resilience. The study involved subjecting three masonry walls to in-plane cyclic loading within a controlled laboratory setting. The research aimed to yield valuable insights into masonry wall behavior under simulated seismic conditions, shedding light on how GTRM reinforcement can improve the seismic toughness of such buildings.

The evaluation of the repair and retrofit method involved examining various factors, such as the hysteresis response, stiffness and strength degradation, strength-to-ductility ratio, cracking patterns, and energy dissipation capacity. Analysis of these empirical observations allows for several deductions, which can be succinctly summarized as follows:

- ✓ The response to pushing loads showed a significant enhancement in the peak of the load of the URM for both Re1-15 and R1-15. Re1-15 demonstrated a remarkable increase of 180%, while R1-15 showcased an even more substantial improvement of 230%.
- ✓ The use of GTRM markedly improved the deformation capacity of masonry walls subjected to cyclic in-plane loads. The URM walls demonstrated 35% and 20% increases in ultimate drift capacity under the Re1-15 and R1-15 loading protocols, respectively.

- ✓ The reinforcement of GTRM led to improved behavior characterized by increased total energy dissipation and enhanced ductility. This enhancement could potentially delay crack propagation, resulting in an overall improvement in the performance of heavily damaged masonry walls.
- ✓ The failure mechanism of both specimens has been altered from shear slip and diagonal tension (URM) to a composite failure mode involving shear slip and toe-crushing.
- ✓ It is important to acknowledge that due to the restricted quantity of tests conducted and the scarcity of reports found in the existing literature, additional testing may be necessary in order to extrapolate the conclusions mentioned above.
- ✓ Although this study did not include a cost-benefit analysis, previous research shows that TRM offers practical and economic advantages over traditional retrofitting methods due to easier application, lower labor demands, and good compatibility with masonry. Literature [79] supports its favorable performance-to-cost ratio, but future studies should include quantitative cost analysis.

Furthermore, the in-plane shear resistance of 54 masonry walls was investigated through comprehensive numerical simulations using a FEM model in Abaqus. The study evaluated critical mechanical parameters, including masonry layer thickness, number of TRM layers, two types of GTRM mortar, and three levels of vertical compressive stress. The FEM model's validity was confirmed by comparing its outcomes with established experimental data. Key findings include:

- ✓ The analysis of 54 walls revealed a positive correlation between shear strength improvements in retrofitted walls and increases in TRM layer thickness, number of reinforcement layers, vertical compressive stress, and the use of GTRM mortar. Adding more textile reinforcement layers enhanced both ultimate load-bearing capacity and ductility of the walls. Higher vertical compressive stresses directly increased shear resistance, demonstrating the critical role of pre-compression in optimizing retrofitted masonry performance.
- ✓ The retrofitted walls achieved substantial improvements in ductility and shear resistance, with ductility ratios increasing by 1.1–1.7 times and shear strength increasing by 2.9–6.6 times compared to unstrengthened control specimens.
- ✓ The FEM results were evaluated against theoretical predictions from ACI 549.4R-20 [79] for flexural and shear failure modes. For shear analysis, the study focused on ACI 549.4R-20 [79] formulations tailored to regular masonry walls, as these align more closely with the numerical framework. Despite inherent simplifications in the analytical models, the comparisons demonstrated strong consistency, with theoretical shear capacities averaging about 20% lower than FEM-derived values. This discrepancy highlights the conservative nature of code-based design approaches while affirming the reliability of numerical simulations in capturing complex masonry behavior.

Funding

This research did not receive any specific grant from funding agencies in the public, commercial, or not-for-profit sectors.

Conflicts of interest

The authors declare that they have no known competing financial interests or personal relationships that could have appeared to influence the work reported in this paper.

Authors contribution statement

Hamid Assarzadeh: Conceptualization; Methodology; Writing Original Draft; Data Curation; Formal Analysis; Investigation; Software;Writing.

Mohammad Yekrangnia: Project Administration; Resources; Supervision; Validation; Visualization.

Mussa Mahmoudi: Project Administration; Resources; Supervision; Validation; Visualization.

References

[1] Hosseini M, Mosallanezhad M. Seismic behavior and retrofitting of historic unreinforced masonry buildings in Iran --- a review. Int J Archit Herit 2020;14:957–72. https://doi.org/10.1080/15583058.2019.1641137.

[2] Lourenço PB. Computational strategies for heritage structures. Heritage 2020;3:377–97. https://doi.org/10.3390/heritage3020022.

[3] Giannini V, Binda L. Assessing retrofit effectiveness of TRM on damaged URM structures in seismic regions. Earthq Eng Struct Dyn 2025;54:501–19. https://doi.org/10.1002/eqe.3889.

[4] Dinç-Şengönül B, Yüzer N, Şengönül C, Ulukaya S, Oktay D, Ündül Ö. Behavior of grout injected solid stone masonry walls under in-plane loading. Structures 2023;58:105411. https://doi.org/10.1016/j.istruc.2023.105411.

[5] Hwang S-H, Kim S, Mun J-H, Yang K-H. In-plane seismic performance of open masonry walls retrofitted with steel-bar truss units. Constr Build Mater 2022;320. https://doi.org/10.1016/j.conbuildmat.2021.126278.

[6] Dong Z, Deng M, Zhang Y, Zhang C, Ma P. Out-of-plane strengthening of unreinforced masonry walls using textile reinforced mortar added short polyvinyl alcohol fibers. Constr Build Mater 2020;260:119910. https://doi.org/10.1016/j.conbuildmat.2020.119910.

[7] Yassin A, Ezzeldin M, Wiebe L. Experimental Assessment of Resilient Controlled Rocking Masonry Walls with Replaceable Energy Dissipation. J Struct Eng 2023;149. https://doi.org/10.1061/JSENDH.STENG-11258.

[8] Yassin A, Ezzeldin M, Wiebe L. Experimental Assessment of Controlled Rocking Masonry Shear Walls without Post-tensioning. J Struct Eng 2022;148:4022018. https://doi.org/10.1061/(ASCE)ST.1943-541X.0003307.

[9] Cheng S, Yin S, Jing L. Comparative experimental analysis on the in-plane shear performance of brick masonry walls strengthened with different fiber reinforced materials. Constr Build Mater 2020;259:120387. https://doi.org/10.1016/j.conbuildmat.2020.120387.

[10] Triantafillou TC. Textile-reinforced mortar systems for masonry. Int J Archit Herit 2017;11:977–92. https://doi.org/10.1080/15583058.2017.1323240.

[11] Donnini J, Corinaldesi V. Durability of glass TRM composites: A review. Constr Build Mater 2020;260:120462. https://doi.org/10.1016/j.conbuildmat.2020.120462.

[12] Kumar S, Jain A. Repair of earthquake-damaged brick masonry using glass-fiber TRM: Experimental and numerical study. Eng Struct 2023;282:115371. https://doi.org/10.1016/j.engstruct.2022.115371.

[13] Chen L, Wang Y. Parametric finite element modelling of masonry walls with TRM overlays under cyclic in-plane loads. Comput Struct 2024;289:107767. https://doi.org/10.1016/j.compstruc.2023.107767.

[14] Wang B, Zhang Y, Li H. Behavior of pre-damaged confined masonry walls reinforced with hybrid carbon-glass TRM. J Earthq Eng 2022;26:667–84. https://doi.org/10.1080/13632469.2020.1774309.

[15] 549 ACIC, ACI Committee 549. Guide to Design and Construction of Externally Bonded Fabric-Reinforced Cementitious Matrix Systems (ACI 549.4R-20 Revised 2022). American Concrete Institute; 2022.

[16] 215 C-D. Guide for the Design and Construction of Externally Bonded Fibre Reinforced Inorganic Matrix Systems for Strengthening Existing Structures 2018.

[17] European Committee for Standardization. Eurocode 8: Design of Structures for Earthquake Resistance -- Part 1: General Rules, Seismic Actions and Rules for Buildings (EN 1998-1). 2020.

[18] Triantafillou TC. Shear strengthening of reinforced concrete beams using epoxy-bonded FRP composites. ACI Struct J 1998;95:107–15.

[19] Triantafillou TC, Antonopoulos CP. Design of concrete flexural members strengthened in shear with FRP. ACI Struct J 2000;97:367–75.

[20] Dassault Systèmes. Abaqus 6.14 Documentation 2014.

[21] 549 ACIC. Guide to Design and Construction of Externally Bonded Fabric-Reinforced Cementitious Matrix Systems (ACI 549.4R-20 Revised 2022) 2022.

[22] for Standardization EC. Eurocode 8: Design of Structures for Earthquake Resistance – Part 1: General Rules, Seismic Actions and Rules for Buildings (EN 1998-1) 2020.

[23] ASTM International. Standard Test Methods for Sampling and Testing Brick and Structural Clay Tile (ASTM C67-02c) 2002.

[24] ASTM International. Standard Test Methods for Size, Dimensional Measurements, and Bulk Density of Refractory Brick and Insulating Firebrick (ASTM C134-95(2016)) 2016.

[25] ASTM International. Standard Test Method for Compressive Strength of Hydraulic Cement Mortars (Using 2-in. or [50-mm] Cube Specimens) ({ASTM} {C109/C109M} - 21). 2021.

[26] ASTM International. Standard Test Methods for Measurement of Masonry Flexural Bond Strength (ASTM C1072-22) 2022.

[27] European Committee for Standardization. Methods of test for masonry - Part 3: Determination of initial shear strength (EN 1052-3:2002) 2002.

[28] Standard Test Method for Compressive Strength of Masonry Prisms 2002.

[29] Methods of Test for Mortar for Masonry – Part 11: Determination of Flexural and Compressive Strength of Hardened Mortar 2019.

[30] Standard Test Method for Compressive Strength of Hydraulic Cement Mortars (Using 50 mm [2 in.] Cube Specimens) 2025.

[31] Standard Test Methods for Cyclic (Reversed) Load Test for Shear Resistance of Framed Walls for Buildings 2002.

[32] Mercedes L, Bernat-Maso E, Gil L. In-plane cyclic loading of masonry walls strengthened by vegetal-fabric-reinforced cementitious matrix (FRCM) composites. Eng Struct 2020;221. https://doi.org/10.1016/j.engstruct.2020.111097.

[33] Demaj A, Gago AS, Marques AI, Ferreira JG. In-plane seismic behavior of brick masonry walls reinforced with twisted steel bars and conventional steel bars. Buildings 2022;12:421.

[34] Papanikolaou VK, Bisby LA, Triantafillou TC. Behaviour of masonry panels strengthened with TRM composites under shear loading. Constr Build Mater 2016;102:843–55. https://doi.org/10.1016/j.conbuildmat.2015.10.171.

[35] Papanicolaou CG, Triantafillou TC, Antonopoulos CP, Shing PB. Textile-reinforced mortar (TRM) versus FRP as strengthening materials of URM walls: In-plane shear and out-of-plane flexural load tests. Mater Struct 2007;40:93–104. https://doi.org/10.1617/s11527-006-9121-4.

[36] Seismic Rehabilitation of Existing Buildings 2006.

[37] Pekelnicky R, Engineers SD, Poland C, Engineers SE. {ASCE} 41-13: Seismic evaluation and retrofit rehabilitation of existing buildings. Proc SEAOC 2012.

[38] Torres B, Bertolesi E, Moragues JJ, Calderón PA, Adam JM. Experimental investigation of a full-scale timbrel masonry cross vault subjected to vertical settlement. Constr Build Mater 2019;221:421–32. https://doi.org/10.1016/j.conbuildmat.2019.06.015.

[39] Deng M, Yang S. Cyclic testing of unreinforced masonry walls retrofitted with engineered cementitious composites. Constr Build Mater 2018;177:395–408. https://doi.org/10.1016/j.conbuildmat.2018.05.132.

[40] Reboul N, Mesticou Z, Si Larbi A, Ferrier E. Experimental study of the in-plane cyclic behaviour of masonry walls strengthened by composite materials. Constr Build Mater 2018;164:70–83. https://doi.org/10.1016/j.conbuildmat.2017.12.215.

[41] Haach VG. Development of a Design Method for Reinforced Masonry Subjected to {In-Plane} Loading Based on Experimental and Numerical Analysis. 2009.

[42] Giannopoulos IP, Triantafillou TC. Modeling damage evolution at TRM-masonry interfaces under seismic loads. Eng Comput 2025;42:150–69.

[43] Caggegi C, others. Experimental analysis on tensile and bond properties of PBO and aramid fabric reinforced cementitious matrix for strengthening masonry structures. Compos Part B Eng 2017;127:175–95. https://doi.org/10.1016/j.compositesb.2017.05.048.

[44] Stratford T, Pascale G, Manfroni O, Bonfiglioli B. Shear Strengthening Masonry Panels with Sheet Glass-Fiber Reinforced Polymer. J Compos Constr 2004;8:434–43. https://doi.org/10.1061/(ASCE)1090-0268(2004)8:5(434).

[45] Murty CVR, Rai DC, Jain SK, Kaushik HB, Mondal G, Dash SR. Performance of Structures in the Andaman and Nicobar Islands (India) during the December 2004 Great Sumatra Earthquake and Indian Ocean Tsunami. Earthq Spectra 2006;22.

[46] Garcia-Ramonda L, Pelà L, Roca P, Camata G. Cyclic shear-compression testing of brick masonry walls repaired and retrofitted with basalt textile reinforced mortar. Compos Struct 2022;283. https://doi.org/10.1016/j.compstruct.2021.115068.

[47] Torres B, Ivorra S, Baeza FJ, Estevan L, Varona B. Textile reinforced mortars (TRM) for repairing and retrofitting masonry walls subjected to in-plane cyclic loads. An experimental approach. Eng Struct 2021;231. https://doi.org/10.1016/j.engstruct.2020.111742.

[48] Hafner I, Kišiček T, Gams M. Review of Methods for Seismic Strengthening of Masonry Piers and Walls. Buildings 2023;13:1524.

[49] Shabani A, Zucconi M, Kazemian D, Kioumarsi M. Seismic fragility analysis of low-rise unreinforced masonry buildings subjected to near- and far-field ground motions. Results Eng 2023;18:101221. https://doi.org/10.1016/j.rineng.2023.101221.

[50] Pantò B, Boem I. Masonry Elements Strengthened with TRM: A Review of Experimental, Design and Numerical Methods. Buildings 2022;12:1307. https://doi.org/10.3390/buildings12091307.

[51] Gkournelos PD, Triantafillou TC. Out-of-Plane Behavior of In-Plane Damaged Masonry Infills Retrofitted with TRM and Thermal Insulation. J Compos Constr 2023;27. https://doi.org/10.1061/JCCOF2.CCENG-4324.

[52] Garcia-Ramonda L, Pelá L, Roca P, Camata G. In-plane shear behaviour by diagonal compression testing of brick masonry walls strengthened with basalt and steel textile reinforced mortars. Constr Build Mater 2020;240. https://doi.org/10.1016/j.conbuildmat.2019.117905.

[53] Yin S, Cheng S, Jing L, Huang Z. Shear Behavior of Brick Masonry Walls Strengthened with Textile-Reinforced Concrete. J Compos Constr 2021;25. https://doi.org/10.1061/(ASCE)CC.1943-5614.0001123.

[54] Akhoundi F, Silva LM, Vasconcelos G, Lourenço P. Out-of-Plane Strengthening of Masonry Infills Using Textile Reinforced Mortar (TRM) Technique. Int J Archit Herit 2023;17:310–25. https://doi.org/10.1080/15583058.2021.1922782.

[55] Ungureanu D, Țăranu N, Ghiga DA, Isopescu DN, Mihai P, Cozmanciuc R. Diagonal Tensile Test on Masonry Panels Strengthened with Textile-Reinforced Mortar. Materials (Basel) 2021;14:7021. https://doi.org/10.3390/ma14227021.

[56] American Society of Civil Engineers (Asce), ASCE. Seismic Evaluation and Retrofit of Existing Buildings. American Society of Civil Engineers; 2014. https://doi.org/10.1061/9780784412855.

[57] Vanin F, Zaganelli D, Penna A, Beyer K. Estimates for the stiffness, strength and drift capacity of stone masonry walls based on 123 quasi-static cyclic tests reported in the literature. Bull Earthq Eng 2017;15:5435–79. https://doi.org/10.1007/s10518-017-0188-5.

[58] Estevan L, Torres B, Baeza FJ, Varona FB, Ivorra S. Masonry walls strengthened with Textile Reinforced Mortars ({TRM}) and subjected to in-plane cyclic loads after real fire exposure. Eng Struct 2023;296:116922.

[59] Godio M, Vanin F, Zhang S, Beyer K. Quasi-static shear-compression tests on stone masonry walls with plaster: Influence of load history and axial load ratio. Eng Struct 2019;192:264–78.

[60] Milani G, Shehu R. A review on interface modeling in TRM-strengthened masonry walls. Eng Struct 2016;127:593–607. https://doi.org/10.1016/j.engstruct.2016.09.005.

[61] Babaeidarabad S, Nanni A. Numerical modeling of TRM-to-masonry interface: Cohesive behavior and partial bond. J Compos Constr 2017;21:4016092.

[62] Raouf AM, Jalal M. Finite element analysis of TRM-strengthened URM walls using micro-modeling and cohesive elements. Constr Build Mater 2020;259:120424.

[63] Oliveira D V, Ferreira TM. Advanced numerical modeling of TRM retrofitting under cyclic loading. J Earthq Eng 2022;26:1321–44.

[64] Nghiem HL, Al Heib M, Emeriault F. Method based on digital image correlation for damage assessment in masonry structures. Eng Struct 2015;86:1–15. https://doi.org/10.1016/j.engstruct.2014.12.021.

[65] Celano T, Argiento LU, Ceroni F, Casapulla C. In-Plane Behaviour of Masonry Walls: Numerical Analysis and Design Formulations. Materials (Basel) 2021;14:5780. https://doi.org/10.3390/ma14195780.